

# Numerical Heat Transfer, Part A: Applications

## An International Journal of Computation and Methodology

ISSN: (Print) (Online) Journal homepage: <https://www.tandfonline.com/loi/unht20>

---

# Heat and mass transfer phenomena for fractal interfacial layer model on metallic-nanomaterials nanofluids flow with chemical reaction effect

Qadeer Raza, Xiaodong Wang, M. Zubair Akbar Qureshi, Ali J. Chamkha & Hassan Ali Ghanzwani

To cite this article: Qadeer Raza, Xiaodong Wang, M. Zubair Akbar Qureshi, Ali J. Chamkha & Hassan Ali Ghanzwani (17 Jan 2024): Heat and mass transfer phenomena for fractal interfacial layer model on metallic-nanomaterials nanofluids flow with chemical reaction effect, Numerical Heat Transfer, Part A: Applications, DOI: [10.1080/10407782.2024.2302961](https://doi.org/10.1080/10407782.2024.2302961)

To link to this article: <https://doi.org/10.1080/10407782.2024.2302961>



Published online: 17 Jan 2024.



Submit your article to this journal [↗](#)





View related articles [↗](#)



View Crossmark data [↗](#)



# Heat and mass transfer phenomena for fractal interfacial layer model on metallic-nanomaterials nanofluids flow with chemical reaction effect

Qadeer Raza<sup>a</sup> , Xiaodong Wang<sup>a</sup>, M. Zubair Akbar Qureshi<sup>b</sup>, Ali J. Chamkha<sup>c</sup> , and Hassan Ali Ghanzwan<sup>d</sup>

<sup>a</sup>School of Mathematics and Statistics, Xi'an Key Laboratory of Scientific Computation and Applied Statistics, Northwestern Polytechnical University, Xi'an, China; <sup>b</sup>Department of Mathematics, Air University, Islamabad, Multan, Pakistan; <sup>c</sup>Faculty of Engineering, Kuwait College of Science and Technology, Doha District, Qatar; <sup>d</sup>Department of Mechanical Engineering, Faculty of Engineering, Jazan University, Kingdom of Saudi Arabia

## ABSTRACT

This study presents a comprehensive investigation into the intricacies of single-phase simulation concerning the behavior of fractal interfacial magnetized metallic chemical-reactive nanoparticles within fluid systems. The research focuses on unraveling the multifaceted phenomena associated with heat and mass transfer in complex nanoscale environments. To achieve this, we employ numerical techniques to address the intricate fluid flow problems that arise due to the presence of these nanoparticles. Fractal complexities are linked to critical phenomena, such as mixing and mass transport, at the turbulent/non-turbulent interface of shear layers and boundary layers. This study primarily concentrates on the phenomena of heat and mass transfer, with a focus on estimating thermal conductivity models that have significant impacts on the flow of metallic nanofluids under convective conditions. The combination of a high thermal conductivity model with a novel interfacial fractal theory reveals a substantial effect on heat and mass transfer enhancement. Furthermore, this research explores hybrid types of porous channel geometries under the combined influence of magnetohydrodynamics and chemical reaction mechanisms in the presence of metallic nanoparticles. A comprehensive numerical analysis of higher-order nonlinear differential equations is conducted, which exposes the flow field's behavior concerning momentum, energy, and mass transfer. These insights are envisioned through single-phase simulations of nanofluids. The influence of the nanoparticles' radius and diameter is found to play a significant role in thermal performance, with nanoparticles ranging from 1% to 8% exhibiting a notable impact on thermal conductivity.

## HIGHLIGHTS

- A new mathematical relation of mass, as well as heat transfer for metallic-nanomaterial being affected by thermal conductivity (T.C.), has been established.
- The important role of the physical number is observed under the effect of T.C. and heat and mass transfer through orthogonal porous surfaces.
- An injection/suction, as well as an expansion/contraction phenomenon related to the porous surface is observed.

## ARTICLE HISTORY

Received 11 October 2023  
Revised 28 November 2023  
Accepted 26 December 2023

## KEYWORDS

chemical reaction; fractal model; heat and mass transfer; metallic-nanoparticle; nano-fluid flow

## 1. Introduction

Fractal models are used to relate complex substances with unpredictable shapes and non-linear dynamic systems in both physical and social spaces. Throughout the study of fractal theory,

**CONTACT** Qadeer Raza  qadeerraza@mail.nwpu.edu.cn  School of Mathematics and Statistics, Xi'an Key Laboratory of Scientific Computation and Applied Statistics, Northwestern Polytechnical University, Xi'an, China

## Nomenclature

$A$	permeability components	$\alpha_{nf}$	nanofluid's thermal diffusivity [ $m^2/s$ ]
$B$	the externals uniforms magnetic fields[T]	$(\rho)_{nf}$	nanofluid density [ $kg/m^3$ ] s
$C$	mass concentrations	$(\nu)_{nf}$	nanofluid's kinematic viscosity [ $m^2/s$ ]
$D$	mass diffusivity coefficients	$Re = \frac{Aa a'}{k_f}$	The permeability Reynolds numbers
$p$	pressure [ $N/m^2$ ]	$Pr = \frac{(\mu_p)_f}{k_f}$	The Prandtl number
$T$	fluids temperatures[K]	$\mu_{nf}$	the nanofluid's dynamic viscosity [ $P_a.s$ ]
$F$	self-similar velocity		
$k_s$	thermals conductivity of solids Fractions [W/m.K]	<b>Greek symbols</b>	
$k_f$	thermals conductivity of the fluids [W/m.K]	$\alpha = \frac{ad(t)}{v_f}$	the wall expansion ratio [ $m^2/s$ ]
$k_{nf}$	thermals conductivity of the Nanofluid [W/m.K]	$\eta$	scaled boundary layer coordinate
$n$	depends on the shape factor through the H-C models	$\chi$	self-similar mass transfer
$\rho_s$	density of the solid fraction [ $kg/m^3$ ] s	$\theta$	self-similar temperature
$c_p$	specific heat capacity of particles [J $kg^{-1}k^{-1}$ ]	$\phi$	nanoparticles volume fractions parameter
$(c_p)_{nf}$	specific heatsof Nano fluid [J $kg^{-1}k^{-1}$ ]	$\mu$	dynamic viscosity [ $P_a.s$ ]
		$\nu$	kinematic viscosity [ $m^2/s$ ]
		$\rho$	density [ $kg/m^3$ ]
		$\sigma$	electric conductivity [ $(m^3A^2)/kg$ ]
		<b>Subscripts</b>	
<b>Dimensionless number</b>		nf	nanofluid
$M = \frac{\sigma B^2 a^2}{\mu}$	magnetic parameter	f	fluid phase
$Sc = \frac{v_f \mu_f}{D}$	Schmidt number	s	solid phase
$K_{cr}$	chemical reaction	$\omega$	conduction at wall
Br	Brinkman number		

fractal models have been intensively practical in logical fields such as mathematics, physical science, financial matters, biology, computer science, cosmology, geomorphology, geography, medication, three-dimensional demography, and phonetics. Unexpectedly, fractal patterns are found everywhere in nature and frequently describe actual physical phenomena like intricate shapes in the fractal geometrically. They contain many important phenomena, such as fractal laser beam production and chemotherapeutic impacts upon microvascular fractal formations, complex environments, molecular complexity, structural complexity of the neural network, the structure of landscapes as well as river networks, aerosol aggregation within Jupiter's atmosphere, the thermodynamic phase change of glass, including fractal patches caused by turbulence that have an impact on phytoplankton biology, and nanoparticle aggregations by researchers Diachenko [1]. A generalized fractal model describing unstructured absorption within permeable mediums having porous forms was recently proposed by Cai et al. [2]. Yang et al. [3] considered the transport singularity of fractional non-Newtonian fluids and suggested a fractal roughness model. Cai et al. [4] investigated recent advances in fractal-based nanofluid and nanoparticle aggregation approaches. A semi-analytical correlation based on a fractal model for pool boiling heat transfers utilizing nanofluids is looked into by Li et al. [5]. Shi et al. [6] looked at the many analytical fractal models that had also been developed to simulate sudden wetting phase imbibition within porous materials with fractal geometry. Miao et al. [7] created a model of fractal relative permeability to describe the movement of water and gas in fracture structures. The probability model was studied by Xu et al. [8] and was shown to depend on saturation, porosity, capillary pressure, microstructural characteristics of porous nanofibers, pores' area fractal dimensions, as well as the tortuous capillaries' fractal dimension. The unique characteristics of the cluster interfacial nanolayer theory for a thermal conductivity-based model are examined by Zubair et al. [9]. The interplay between the metallic oxide nanomaterials' fractal flow and the base fluid is investigated under the effect of magnetohydrodynamics. Yan et al. [10] introduce a novel approach to modeling the rapid

diffusion of chloride in concrete through a space fractal derivative temperature model. They successfully obtain an explicit solution using the complementary error function. Furthermore, the current study introduces a time-space Hausdorff derivative model, which effectively characterizes the transport of solutes in aquifers or the flow of water in heterogeneous porous media. In this innovative model, both time and space Hausdorff derivatives are defined on non-Euclidean fractal metrics, each employing power law scaling transforms. These transforms establish connections between the temporal and spatial complexities that arise during the transport process [11, 12].

The study of nanofluids is indispensable for civil, mechanical, and chemical engineering as well as for scientific purposes in the fields of hydroelectric, thermal power, and nuclear energy. The inclusion of thermal conductivity is the main hurdle in the transfer of movable nanofluids in the engineering and technological departments. Industrialized uses of combined heat and mass transfer, including chemical reactions and thermal diffusion, have significant and fruitful applications. To control the distribution of energetic forces, Chen et al. [13] carefully considered the thermodynamic equilibrium involving cumulative heat transfer as well as mass growth along the unsaturated, affected, and saturated conduction. Thermal diffusion, induced magnetic field flow, as well as the magnetic hydrodynamics (MHD) impact on mass transfer as well as heat transfer flow *via* an exponentially extending sheet of vertical alignment, mostly with the involvement of thermally radiating as well as a dissipative influence, were all topics covered and analyzed by Poddar et al. [14]. Narahari and Dutta [15] investigate the consequences of both heat and mass transfer across a movable vertical plate with a ramping wall temperature, and they provide an appropriate analytical approach to the problem. Allah [16] considered the effect of porous media on heat as well as mass transmission at the interface of two viscous fluids. Despite the availability of packed-bed bioreactors for consistent fermentation, there haven't been many attempts in recent years to experimentally quantify the heat as well as mass transmission coefficients between both the particle and air stages. Finkler et al. [17] looked at water and heat transmission using bioprocesses that are packed-bed and involve solid-state fermentation. The impact of the null value of mass flux on the measurement of temperatures as well as the mass flow of nanofluid flow within a hole under a magnetic field was examined by Reddy and Sreedevi [18]. With magnetic hydrodynamic (MHD) natural convection of Newtonian warming and continuous soluble attentiveness inserted in the porous channel, Shah et al. [19] examined the heat as well as mass transmission flow relating to a non-compressible fluid having viscosity over endless vertical plates. Mao et al. [20] examined changes in mass transfer and heat transmission during conventional solvent extraction as well as microwave-assisted solvent separation. Chen et al. [13] investigated the dispersion of driving forces throughout the thermodynamic equilibrium of simultaneous mass transfer along with heat transmission procedures across unsaturated, saturated, and supersaturated situations of humid air by using individual air insertion as well as removal. Once heated in an environment of gases with high temperatures under circumstances of dehydration, Kuznetsov et al. [21] identified the characteristics of heat as well as mass transmission processes in a dense covering of moist timber biomass. Chen et al. [22] analyzed the heat as well as mass transmission performances of new absorbers made up of a bundle of S-shaped capillary coils and conducted experiments to develop a workable ammonia-water absorption system in various settings. The effect of the lightness proportion on that two-dimensional normal convective mass as well as heat exchange caused in a layered permeable cavity filled with Newtonian liquid within an angled square bi-L-shaped hole was investigated by Abdelkrim and Mahfoud [23].

In the field of nanoscience, metallic nanoparticles are employed in several applications, especially within the medical and biological sciences. Gold nanoparticles with a diameter of 1nm would move across the cell nucleus as well as the membranes to interrelate with DNA. Gao et al. [24] found that gold nanoparticles with a diameter of 18 nm have great penetration without cytotoxicity. Shen et al. [25] observed the constant spinning of mesoscopic metal particle trimers, which are visually constrained by a powerful optical vortex that is spirally polarized. To study the existence of bioconvection in a flow of convective nanofluids harboring gyro-tactic

microorganisms having chemically reactive substances, Rao et al. [26] installed an isothermal upright cone in a permeable material. The coupled conjugate heat and mass transport phenomena having effects on heat generation and chemical reactions in a vertical hollow cylinder exploiting MHD laminar mixed convective flow are considered by Saidoune et al. [27]. The effects of viscous dispersion upon high-order chemical processes on highly conductive MHD nanofluids were numerically investigated by Gopal et al. [28]. Minakov et al. [29] researched experimentally the involuntary turbulence convection within water-based nanofluids with zirconium oxide ( $ZrO_2$ ) nanoparticles in channels and smooth tubes with wall heat transfer enhancements. The lattice Boltzmann technique used by Mohebbi et al. [30] to investigate the effects of modifying various parameters, like the volume fraction of solid,  $Re$ , and Heat flow was pushed by intervals of nanofluids in a medium with prolonged surfaces connected to the sides. In a symmetric wavy medium, Dormohammadi et al. [31] quantitatively investigated the impact of physical parameters, including nanoparticle distribution inside the base fluid, upon heat transmission and energy generation. Wakif et al. [32] studied the effect of thermal radiation as well as magnetic fields on the unstable ordinary Couette heat flux in Cu-water nanofluids enclosed between two infinite vertical plates. Sheikholeslami et al. [33] demonstrated turbulent convective nanofluid flows with helical turbulence within a porous channel. Hayat et al. [34] considered radiative micro-polar nanofluids with crucial Buongiorno model slip mechanisms. Liang and Mudawar [35] discussed the main features of the fact that among the fluids with boiling thermal conductivity were the nanofluids. Hussain et al. [36] investigated the thermally induced unstable flow of viscous nanofluid owing to porous media having opposing movements of the sidewalls using the Beaver-Joseph slip condition. Under radiative temperatures with no-slip boundary conditions on the walls of the channel, the effect of sidewall elasticity mostly on the peristaltic flow of MHD in an Eyring-Powell nanofluid is evaluated by Nisar et al. [37]. Gowda et al. [38] looked at the 2D, immiscible movement of nanofluid through a curving, stretched surface coiled in a circle. The Koo-Kleinstreuer and Li (KKL) model is used to examine the effects of nanoparticle Cuos dispersal in base fluid water on flows, TC, as well as transfers of mass under the influence of Cattaneo-Christov heat flux as well as the energy of activation. The Altanganas-Baleanus Caputo (ABCs) sense is used by Arafa et al. [39] on unsteady MHD bio-convection nanofluid skin friction flows caused by gyrotactic microorganisms.

The primary goal of the current study is to describe the numerical modeling of thermal conductivity with the help of nanoparticle aggregation, interfacial nanolayer ordinary heat conduction, and mass transfers of compact nanofluid flow through a channel of porous walls with chemical reactions. These will be validated and represented by a graphical figure depicting the effects of wall expansion ratio, magnetic parameters, nanoparticle volume fractions, permeability Reynolds numbers, and Brinkman numbers on the flow and thermal characteristics. Additionally, we will suggest velocity, temperature, and mass characteristics for these Reynolds numbers, as well as loosening and contracting factors with a given quantity of nanoparticles when a nanolayer is present. The governing equation will be transformed using the similarity transformations approach into numerically calculated, highly nonlinear ordinary differential equations.

The integration of a high thermal conductivity model with an innovative interfacial fractal theory reveals a significant enhancement in heat and mass transfer. Additionally, the study extends its exploration to hybrid porous channel geometries, considering the combined influence of magnetohydrodynamics (MHD) and chemical reaction mechanisms in the presence of metallic nanoparticles. The comprehensive numerical analysis of higher-order nonlinear differential equations offers insights into the flow field's behavior concerning momentum, energy, and mass transfer. Through single-phase simulations of nanofluids, the research unveils the substantial impact of nanoparticles' radius and diameter on thermal performance, particularly within the range of 1–8%. This research provides valuable insights for understanding and optimizing nanofluid behavior, paving the way for advancements in various technological applications.

## 2. Mathematical modelling

The layered structure shaped by the fluid particles close to the nanoparticle surface behaves like a solid and has magnitudes of nanometers. The thermal conductivity (T.C.) is amplified by the construction of the nanolayer between nanoparticles and stacks of fluids. Bulk fluids, a group of firm nanoparticles, as well as a nanolayer that encapsulates the grouping of nanoparticles, are all present. As a result, as per fractal modeling, the thermal conductivity depends on the size of the groups, the width of the nanolayers, as well as the thermal resistance of the interfacial planes between both the faces of the nanoparticles and the fluid aggregates. Bruggeman combines nanoparticle aggregation to determine the thermal conductivity and provides

$$\frac{k_{nf}}{k_f} = \frac{(k_a + 2k_f) - 2(k_f - k_a)\phi_a}{(k_a + 2k_f) + (k_f - k_a)\phi_a} \quad (1)$$

In which the Bruggeman models are used to calculate the values of  $k_a$ , the thermal aggregation's conductivity as the T.C. determiner is the imperative thermophysical property that impacts these nano-fluid heat transfer rates. The T.C. upgrade of nanofluids can be credited to a few factors, for example, volume parts, temperatures, material sort, and size and shape factors. The popular Maxwell models were the first to be utilized to determine the thermal conductivity of miniature or small-scale particle suspensions at limited-volume suspension convergences. Nonetheless, Maxwell's models are used for research purposes with test discoveries due to their simplicity in determining the nanofluid's thermal conductivity. The condition of particles is not taken into account in Maxwell's model. An all-encompassing adaptation of Maxwell's models suggested by Hamilton-Crossers incorporates a variable " $n$ " known as shape factors. For instance,  $n = 3$  represents circular particles,  $n = 4.9$  speaks to needles, and  $n = 6$  represents poles. Diverse-formed nanoparticles have several uses and are particularly prominent in the clinical sciences. The Hamilton-Crossers (H-Cs) models are the most well-known models for the compelling nanofluids of warm conductivity presented by Das et al. [40].

$$k_{nf} = k_f \left[ \frac{k_a + (n-1)k_f - (n-1)(k_f - k_a)\phi}{k_a + (n-1)k_f + (k_f - k_a)\phi} \right] \quad (2)$$

Fractal nanolayers can be formed by certain nanoparticle arrangements or materials that exhibit fractal patterns. These patterns are often irregular and complex, with details at smaller scales resembling the overall structure (Figure 1). The presence of fractal nanolayer can influence

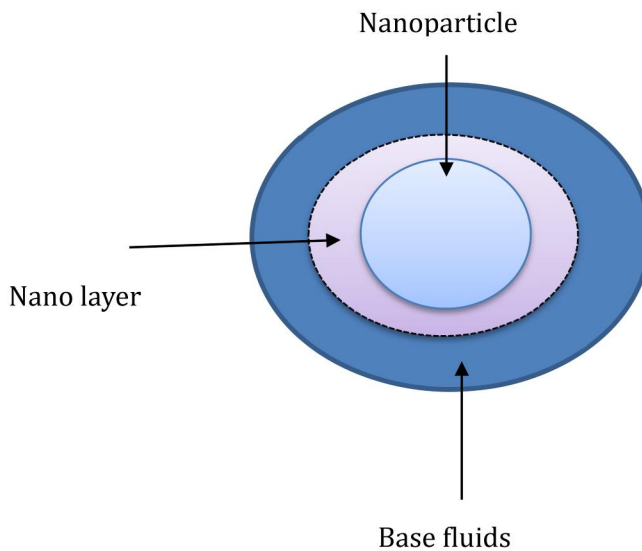


Figure 1. Nanolayer physical model.

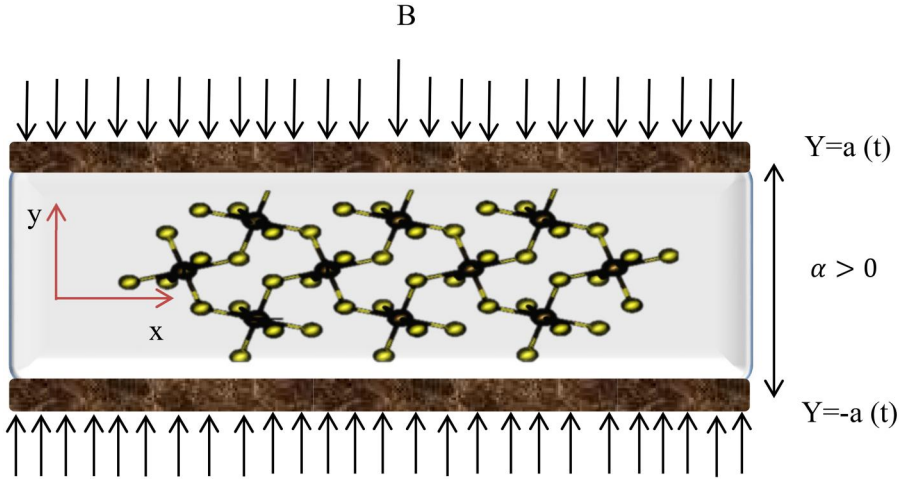


Figure 2. Physical model of permeable channel for the expansion  $\alpha > 0$ .

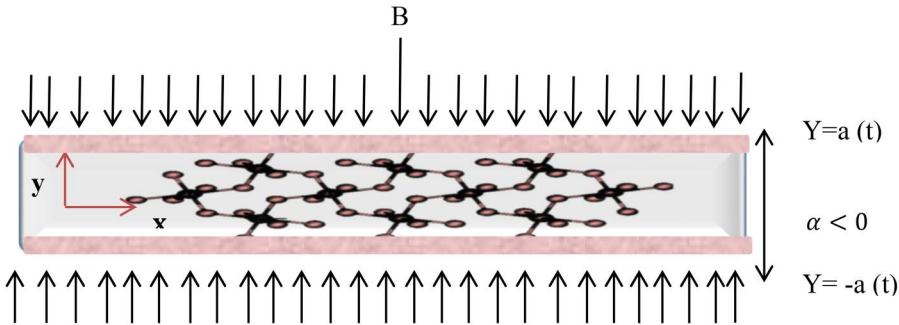


Figure 3. Physicals' models of permeable channel for the contraction  $\alpha < 0$ .

various properties of materials, such as their mechanical, electrical, or thermal behavior, in ways that differ from more conventional, non-fractal structures. In scientific research and applications, understanding and manipulating fractal nanolayers can be important for controlling and optimizing the properties of nanomaterials. For instance, in studies involving fluid dynamics or surface interactions, the presence of fractal nanolayers may affect phenomena like adhesion, permeability, or heat transfer at the nanoscale. Regarding nanoparticles that are spherical,  $\psi = 1$  or  $n = 3$ , whereas for cylindrical nanoparticles,  $\psi = 0.5$  or  $n = 6$ . Figures 2 and 3 show the schematic diagram of the problem. In efforts to imagine suitable frameworks for the functional thermal conductivity along with the viscosity of nanofluids, numerous speculative works are debated [41–49]. The thermal conductivity of nanolayers is

$$k_{\text{nlfid}} = \frac{(k_{s1} - k_{\text{nlr}})\phi k_{lr}(\lambda_2^2 - \lambda_1^2 + 1) + (k_{s1} + k_{\text{nlr}})\lambda_2^2(\phi\lambda_1^2(k_{\text{nlr}} - k_{\text{bf}}) + k_{\text{bf}})}{\lambda_2^2(k_{s1} + k_{\text{nlr}}) - (k_{s1} - k_{\text{nlr}})\phi(\lambda_2^2 + \lambda_1^2 - 1)} k_{\text{bf}} \quad (3)$$

Here,  $\lambda_1 = 1 + \frac{h}{r}$ ,  $\lambda_2 = 1 + \frac{h}{2r}$ ,  $h$  shows the nanolayer thickness, and  $r$  represents the radius of the nanoparticle, shows a physical model in a nanolayer with base fluid and nanoparticles  $k_{\text{nlr}} = 3k_{\text{bf}}$ , are signified by nanolayer, nanolayer fluid, and base fluid thermal conductivity [50].

$$k_{\text{nf}} = \frac{\left(\frac{k_a}{k_f} + 2\right) - 2\left(1 - \frac{k_a}{k_f}\right)\phi}{\left(\frac{k_a}{k_f} + 2\right) + \left(1 - \frac{k_a}{k_f}\right)\phi} \quad (4)$$

$$\frac{k_a}{k_f} = \frac{1}{4} \left( (3\phi - 1) \frac{k_s}{k_f} + (2 - 3\phi) \right) + \sqrt{\left( \left( (3\phi - 1) \frac{k_s}{k_f} + (2 - 3\phi) \right)^2 + 8 \frac{k_s}{k_f} \right)} \quad (5)$$

$$\phi = \left( \frac{r_a}{r_p} \right)^{D^* - 3}$$

Sindhu and Giresha [51] investigated the widely accepted values of  $D^* = 1.8$ ,  $\frac{r_a}{r_p} = 3.34$  represent high-rate flows.

The coordinate reference frameworks put these beginnings at the center of the media, with permeable walls that permit the fluids to enter as well as exit throughout successive current problems.

$$\frac{\partial \mathbf{u}}{\partial \mathbf{x}} + \frac{\partial \mathbf{v}}{\partial \mathbf{y}} = 0 \quad (6)$$

$$\left( \frac{\partial \mathbf{u}}{\partial t} + \mathbf{u} \frac{\partial \mathbf{u}}{\partial \mathbf{x}} + \mathbf{v} \frac{\partial \mathbf{u}}{\partial \mathbf{y}} \right) + \frac{1}{\rho_{nf}} \frac{\partial \mathbf{p}}{\partial \mathbf{x}} = \frac{\mu_{nf} \nabla^2 \mathbf{u}}{\rho_{nf}} - \frac{\sigma \beta^2}{\rho_{nf}} \mathbf{u} \quad (7)$$

$$\left( \frac{\partial \mathbf{v}}{\partial t} + \mathbf{u} \frac{\partial \mathbf{v}}{\partial \mathbf{x}} + \mathbf{v} \frac{\partial \mathbf{v}}{\partial \mathbf{y}} \right) + \frac{1}{\rho_{nf}} \frac{\partial \mathbf{p}}{\partial \mathbf{y}} = \frac{\mu_{nf} \nabla^2 \mathbf{v}}{\rho_{nf}} \quad (8)$$

$$\left( \frac{\partial \Gamma}{\partial t} + \mathbf{u} \frac{\partial \Gamma}{\partial \mathbf{x}} + \mathbf{v} \frac{\partial \Gamma}{\partial \mathbf{y}} \right) - \frac{\mu_{nf}}{(\rho C_p)_{nf}} \left( \frac{\partial \mathbf{u}}{\partial \mathbf{y}} \right)^2 = \alpha_{nf} \nabla^2 \Gamma \quad (9)$$

$$\left( \frac{\partial \mathbf{C}}{\partial t} + \mathbf{u} \frac{\partial \mathbf{C}}{\partial \mathbf{x}} + \mathbf{v} \frac{\partial \mathbf{C}}{\partial \mathbf{y}} \right) + k_0 (\mathbf{C} - \mathbf{C}_2) = D \nabla^2 \mathbf{C} \quad (10)$$

Chen et al. [52] by adding the impacts of nanoparticle aggregation and Maxwells-Bruggemans to get the effective thermal conductivity. The updated Krieger-Dougherty approach was deemed adequate for a more practically reliable thickness estimation of ethylene glycol-based titanium nanofluids.

$$\mu_{nf} = \left( 1 - \frac{\phi_a}{\phi_m} \right) ([n] \phi_m) \text{ and } \phi_m = \phi \left( \frac{r_a}{r_p} \right)^{3-D^*} \quad (11)$$

Here,  $\phi_m$  are these extremes volumes fractions,  $[n]$  is Einstein's coefficients, and  $\phi_a$  is the effective volume fractions of assemble, anywhere, in which  $D^*$  are the fractals indexes.

By using the above entities, we get

$$\frac{\mu_{nf}}{\mu_f} = \left( 1 - \frac{\phi}{\phi_m} \left( \frac{r_a}{r_p} \right)^{3-D^*} \right)^{([n] \phi_m)} \quad (12)$$

Mackolil and Mahanthesh [53] researched the commonly established values of  $D^* = 1.8$ ,  $\frac{r_a}{r_p} = 3.34$ , and  $\phi_m = 0.605$  signify the high rates flow. For these monodisperse system,  $[n] = 2.5$

$$\left\{ \begin{array}{l} \alpha_{nf} = \frac{k_{nf}}{(\rho C_p)_{nf}}, \quad \frac{\rho_{nf}}{\rho_f} = (1 - \phi) + \phi \frac{\rho_s}{\rho_f} \\ \frac{(\rho C_p)_{nf}}{(\rho C_p)_f} = (1 - \phi) + \phi \frac{(\rho C_p)_s}{(\rho C_p)_f}, \quad \nu_{nf} = \frac{\mu_{nf}}{\rho_{nf}}, \quad \alpha_{nf} = \frac{k_{nf}}{(\rho C_p)_{nf}}, \end{array} \right. \quad (13)$$

The boundary conditions are

$$\left\{ \begin{array}{l} u = 0 : v = -Aa'(t), \text{ at } y = -a(t) \text{ when } T = T_1 \text{ and } C = C_1 \\ u = 0 : v = Aa'(t), \text{ at } y = a(t) \text{ when } T = T_2 \text{ and } C = C_2 \end{array} \right\} \quad (14)$$

Here,  $A$  is the wall porous element, and the primes signify the derivatives concerning the time ( $t$ ).

We have used the resulting similarity transform.

$$\left\{ \eta = \frac{y}{a}, \quad u = -\frac{xy_f}{a^2} F_\eta(\eta, t), \quad v = \frac{y_f}{a} F(\eta, t), \quad \theta = \frac{T - T_2}{T_1 - T_2}, \quad \varrho(\eta) = \frac{C - C_2}{C_1 - C_2} \right\} \quad (15)$$

To reduce Eqs. (6)–(9), the following systems of ordinary nonlinear differentials Equations are then added:

$$\frac{v_{nf}}{v_f} F_{\eta\eta\eta\eta} + \alpha(3F_{\eta\eta} + \eta F_{\eta\eta\eta}) - FF_{\eta\eta\eta} + F_\eta F_{\eta\eta} - \frac{\rho_f}{\rho_{nf}} MF_{\eta\eta} - \frac{a^2}{v_f} F_{\eta\eta t} = 0, \quad (36)$$

$$\frac{\alpha_{nf}}{v_f} \theta_{\eta\eta} - a^2 \theta_t + \theta_\eta(\eta\alpha - F) + \left( \frac{\mu}{\rho C_p} \right)_{nf} \left( \frac{v^2 x^2}{a^6} F_{\eta\eta}^2 \right) = 0, \quad (47)$$

$$\frac{D}{v_f} \chi_{\eta\eta} - a^2 \chi_t + \chi_\eta \eta \alpha - F \chi_\eta - K_0 \chi \frac{a^2}{v_f} = 0, \quad (58)$$

Whereas the boundary conditions are

$$\begin{aligned} \eta = -1 : F = -Re : F_\eta = 0, \quad \theta = 1 \text{ and } \chi = 1, \\ \eta = 1 : F = Re : F_\eta = 0, \quad \theta = 0 \text{ and } \chi = 0. \end{aligned} \quad (19)$$

Here,  $T_1$  and  $T_2$  show the temperature while  $C_1$  and  $C_2$  represent the concentrations of these lower and upper walls. Permeable channels with  $T_1 > T_2$  and  $C_1 > C_2$ , respectively. The pace must suggest is consistent with the continuity Eq. (5). Also we found the cases when  $\alpha$  is a constant by following Majdalani et al. [54] and  $\theta_\eta = F_{\eta\eta t} = \chi_t = 0$  so that's  $F = F(\eta)$  and  $\theta = \theta(\eta)$ . Thus we have the equations that follow:

$$\left( \left( \frac{\mu_{nf}}{\mu_f} \right) \left( \frac{\rho_{nf}}{\rho_f} \right) \right) F_{\eta\eta\eta\eta} + \alpha(3F_{\eta\eta} + \eta F_{\eta\eta\eta}) - FF_{\eta\eta\eta} + F_\eta F_{\eta\eta} - \frac{\rho_f}{\rho_{nf}} MF_{\eta\eta} = 0 \quad (20)$$

$$\frac{\alpha_{nf}}{v_f} \theta_{\eta\eta} + \theta_\eta(\eta\alpha - F) + \left( \frac{\mu}{\rho C_p} \right)_{nf} \left( \frac{v^2 x^2}{a^6} F_{\eta\eta}^2 \right) = 0, \quad (21)$$

$$\frac{D}{v_f} \chi_{\eta\eta} + \chi_\eta(\eta\alpha - F) - K_0 \chi \frac{a^2}{v_f} = 0, \quad (22)$$

Finally, adjusting  $F = fRe$ , [47], we have

$$\left( \left( \frac{\mu_{nf}}{\mu_f} \right) \left( \frac{\rho_{nf}}{\rho_f} \right) \right) f_{\eta\eta\eta\eta} + \alpha(3f_{\eta\eta} + \eta f_{\eta\eta\eta}) - Re(ff_{\eta\eta\eta} - f_\eta f_{\eta\eta}) - \frac{\rho_f}{\rho_{nf}} Mf_{\eta\eta} = 0, \quad (23)$$

$$\frac{K_{nf}}{K_f} \theta_{\eta\eta} + \frac{(\rho C_p)_{nf}}{(\rho C_p)_f} Pr \cdot \theta_\eta((\eta\alpha) - Re f) + (1 - \phi)^{-2.5} Br Re^2 f_{\eta\eta}^2 = 0, \quad (24)$$

$$\chi_{\eta\eta} + Sc \cdot \chi_\eta((\eta\alpha) - fRe) - C \cdot \chi(\eta) = 0, \quad (25)$$

Which are then converted into the form of the volume's fractions of nanoparticles

$$\begin{aligned} & \frac{1}{(1 - 7.0264\phi)^{(-1.5125)} \left( (1 - \phi) + \phi \frac{\rho_s}{\rho_f} \right)} (f_{\eta\eta\eta\eta} - f_{\eta\eta}) + \alpha(3f_{\eta\eta} + \eta f_{\eta\eta\eta}) - Re(ff_{\eta\eta\eta} - f_\eta f_{\eta\eta}) \\ & - \frac{1}{\left( (1 - \phi) + \phi \frac{\rho_s}{\rho_f} \right)} Mf_{\eta\eta} = 0, \end{aligned} \quad (26)$$

$$\begin{aligned}
 & \left( \frac{1}{4} \left( (3\phi - 1) \frac{k_s}{k_f} + (2 - 3\phi) \right) + \sqrt{\left( \left( (3\phi - 1) \frac{k_s}{k_f} + (2 - 3\phi) \right)^2 + 8 \frac{k_s}{k_f} \right) + 2} \right) \\
 & - 2 \left( 1 - \frac{1}{4} \left( (3\phi - 1) \frac{k_s}{k_f} + (2 - 3\phi) \right) + \sqrt{\left( \left( (3\phi - 1) \frac{k_s}{k_f} + (2 - 3\phi) \right)^2 + 8 \frac{k_s}{k_f} \right)} \right) \phi \\
 & \frac{\left( \frac{1}{4} \left( (3\phi - 1) \frac{k_s}{k_f} + (2 - 3\phi) \right) + \sqrt{\left( \left( (3\phi - 1) \frac{k_s}{k_f} + (2 - 3\phi) \right)^2 + 8 \frac{k_s}{k_f} \right) + 2} \right)}{\left( \frac{1}{4} \left( (3\phi - 1) \frac{k_s}{k_f} + (2 - 3\phi) \right) + \sqrt{\left( \left( (3\phi - 1) \frac{k_s}{k_f} + (2 - 3\phi) \right)^2 + 8 \frac{k_s}{k_f} \right)} \right)} \theta_{\eta\eta} \\
 & + \left( 1 - \frac{1}{4} \left( (3\phi - 1) \frac{k_s}{k_f} + (2 - 3\phi) \right) + \sqrt{\left( \left( (3\phi - 1) \frac{k_s}{k_f} + (2 - 3\phi) \right)^2 + 8 \frac{k_s}{k_f} \right)} \right) \phi \\
 & + \left( (1 - \phi) + \phi \frac{(\rho C_p)_s}{(\rho C_p)_f} \right) (\text{Pr} \cdot \theta_{\eta} ((\eta\alpha) - \text{Re} f)) + \frac{1}{(1 - 7.0264\phi)^{(-1.5125)}} \cdot \text{Br} \cdot \text{Re}^2 \cdot f_{\eta\eta}^2 = 0, \tag{27} \\
 & \chi_{\eta\eta} + \chi_{\eta} (\text{Sc}(\eta\alpha) - \text{Re}f) - C \cdot \chi(\eta) = 0 \tag{28}
 \end{aligned}$$

With these boundary conditions

$$\begin{cases} \eta = -1 : f = -1 : f_{\eta} = 0, \theta = 1 \text{ and } \chi = 1, \\ \eta = 1 : f = 1 : f_{\eta} = 0, \theta = 0 \text{ and } \chi = 0 \end{cases} \tag{29}$$

Here,  $\alpha = \frac{sa(t)a'(t)}{sv}$  is a non-dimensional, time-dependent relaxation/contraction measure that, if positive, indicates contraction, and if negative, indicates relaxation. The permeability Reynolds number changes to  $Re = \frac{Aa(t)a'(t)}{sv} < 0s$  in the case of suction and  $Re = \frac{Aa(t)a'(t)}{sv} > 0$  for the injection,  $\text{Br} = \text{Ec}^* \text{Pr}$  denoted by Brinkman number,  $C = K_0 \frac{a^2}{v_f}$  is denoted chemical reaction parameter and  $M = \frac{\sigma \beta^2 a^2}{\mu_f}$  is magnetic field parameter.

$$\begin{aligned}
 & \left\{ \begin{aligned} S_1(\phi) &= (1 - 7.0264\phi)^{(1.5125)}, \quad S_2(\phi) = \left( (1 - \phi) + \phi \frac{\rho_s}{\rho_f} \right)^{-1} \\ S_3(\phi) &= \left( (1 - \phi) + \phi \frac{(\rho C_p)_s}{(\rho C_p)_f} \right) \end{aligned} \right\} k(\phi) \\
 & \left( \frac{1}{4} \left( (3\phi - 1) \frac{k_s}{k_f} + (2 - 3\phi) \right) + \sqrt{\left( \left( (3\phi - 1) \frac{k_s}{k_f} + (2 - 3\phi) \right)^2 + 8 \frac{k_s}{k_f} \right) + 2} \right) \\
 & - 2 \left( 1 - \frac{1}{4} \left( (3\phi - 1) \frac{k_s}{k_f} + (2 - 3\phi) \right) + \sqrt{\left( \left( (3\phi - 1) \frac{k_s}{k_f} + (2 - 3\phi) \right)^2 + 8 \frac{k_s}{k_f} \right)} \right) \phi \tag{30} \\
 & = \frac{\left( \frac{1}{4} \left( (3\phi - 1) \frac{k_s}{k_f} + (2 - 3\phi) \right) + \sqrt{\left( \left( (3\phi - 1) \frac{k_s}{k_f} + (2 - 3\phi) \right)^2 + 8 \frac{k_s}{k_f} \right) + 2} \right)}{\left( \frac{1}{4} \left( (3\phi - 1) \frac{k_s}{k_f} + (2 - 3\phi) \right) + \sqrt{\left( \left( (3\phi - 1) \frac{k_s}{k_f} + (2 - 3\phi) \right)^2 + 8 \frac{k_s}{k_f} \right)} \right)} \\
 & + \left( 1 - \frac{1}{4} \left( (3\phi - 1) \frac{k_s}{k_f} + (2 - 3\phi) \right) + \sqrt{\left( \left( (3\phi - 1) \frac{k_s}{k_f} + (2 - 3\phi) \right)^2 + 8 \frac{k_s}{k_f} \right)} \right) \phi
 \end{aligned}$$

Putting (30) then Eqs. (26)–(28) becomes

$$[\mathbf{S}_1(\phi)\mathbf{S}_2(\phi)](f_{\eta\eta\eta\eta} - f_{\eta\eta}) + \alpha(3f_{\eta\eta} + \eta f_{\eta\eta\eta}) - \mathbf{Re}(ff_{\eta\eta\eta} - f_{\eta}f_{\eta\eta}) - \mathbf{S}_2(\phi) \cdot \mathbf{M}f_{\eta\eta} = 0, \quad (31)$$

(

$$\mathbf{k}(\phi)\theta_{\eta\eta} + \mathbf{S}_3(\phi)(\mathbf{Pr}(\eta\alpha) - \mathbf{Re} f)\theta_{\eta} + \mathbf{S}_1(\phi) \cdot \mathbf{Br} \cdot \mathbf{Re}^2 \cdot f_{\eta\eta}^2 = 0, \quad (32)$$

$$\chi_{\eta\eta} + \chi_{\eta} \mathbf{Sc}(\eta\alpha - \mathbf{Re} f) - \mathbf{C} \cdot \chi(\eta) = 0, \quad (33)$$

### 3. Numerical procedure

A mathematical strategy, the 4th-order Runge-Kutta technique alongside the shootings approach can be applied to solving the layout of nonlinear ODEs using initial conditions (30) and the combination conditions for Eqs. (31–33).

The 4th-order Runge-Kutta technique, coupled with the shooting approach, stands as a robust numerical method widely employed in solving ordinary differential equations (ODEs) and boundary value problems. By leveraging the Runge-Kutta method's accuracy and stability, combined with the shooting approach's iterative nature, this hybrid technique efficiently computes solutions for complex systems of ODEs, especially those involving boundary conditions. Its versatility and precision make it a go-to tool in scientific and engineering domains, enabling the exploration, and understanding of intricate dynamic systems and phenomena.

Before using the mathematical technique, we organize the supervising ODEs into a set of first-order ODEs, as shown below:

We put  $r_1 = f[\eta]$ ,  $r_2 = f'[\eta]$ ,  $r_3 = f''[\eta]$ ,  $r_4 = f'''[\eta]$ ,  $r_5 = \theta[\eta]$ ,  $r_6 = \theta'[\eta]$ ,  $r_7 = \chi[\eta]$ ,  $r_8 = \chi'[\eta]$  Eqs. (30–32),

$$\left\{ \begin{array}{l} r'_4 = (\mathbf{S}_1(\phi)\mathbf{S}_2(\phi))^{-1}[\mathbf{S}_2(\phi)\mathbf{M}r_3 + \mathbf{Re}(r_1r_4 - r_2r_3) - \alpha(3r_3 + \eta r_4)], \\ r'_6 = -\mathbf{K}(\phi)^{-1}[\mathbf{S}_3(\phi)(\eta\alpha - \mathbf{Re}r_1)r_6 + \mathbf{S}_1(\phi)\mathbf{Br} \cdot \mathbf{Re}^2 \cdot r_3^2]Pr, \\ r'_8 = \mathbf{C}(r_7) - \mathbf{Sc}(\eta\alpha - \mathbf{Re} r_1)r_8 \end{array} \right\} \quad (34)$$

With the following mandatory boundary conditions:

$$\left\{ \begin{array}{l} r_1(-1) = -1, r_2(-1) = 0, r_5(-1) = 1, r_7(-1) = 1, r_1(-1) = x_1, r_2(-1) = x_2 \\ , r_3(-1) = x_3, r_4(-1) = x_4. \end{array} \right\} \quad (35)$$

Here,  $x_1$ ,  $x_2$ ,  $x_3$ , and  $x_4$  are missing initial conditions. Subsequently, at these stages, a shooting method is viable to discover the obscure initial conditions with the lowest computational costs.

## 4. Practical and engineering interest

Skin friction as well as Nusselt numbers are basic quantities that are significant in production goals to simulate equipment. These variables have all been determined for each porous medium.

### 4.1. Skin friction coefficients

The skin friction factors of the bottom and upper sidewalls of channels are represented by the  $Cf_1$  as well as  $Cf_2$  and are stated as

$$Cf_1 = \frac{\xi_{yx}|_{y=-a(t)}}{\rho_f(a'A)^2} = \frac{1}{(1 - 7.0264\phi)^{(-1.5125)}} f''(-1)$$

$$Cf_2 = \frac{\xi_{yx}|_{y=a(t)}}{\rho_f(a'A)^2} = \frac{1}{(1 - 7.0264\phi)^{(-1.5125)}} f''(-1)$$

here  $\xi_{yx}$  is shear stress present at the lower and the higher channel walls.

$$\xi_{yx} = \mu_{nf} \left( \frac{\partial u}{\partial y} \right) \Big|_{y=-a(t)} = \frac{\mu_f}{(1 - 7.0264\phi)^{(-1.5125)}} f''(-1)$$

$$\tau_{yx} = \mu_{nf} \left( \frac{\partial u}{\partial y} \right) \Big|_{y=a(t)} = \frac{\mu_f}{(1 - 7.0264\phi)^{(-1.5125)}} f''(1)$$

#### 4.2. Nusselt numbers

The Nusselt number of values one acts for heat transfer by pure conductions. Calculating the heat transfer amount only at the channel's bottom and top walls (Nusselt numbers)  $Nu_1$  and  $Nu_2$  are given us

$$Nu_1 = \frac{as_z}{k_f(t_1 - t_2)} \Big|_{y=-a(t)} = -\frac{k_{nf}}{k_f} \theta'(-1)$$

$$Nu_2 = \frac{as_z}{k_f(t_1 - t_2)} \Big|_{y=a(t)} = -\frac{k_{nf}}{k_f} \theta'(1)$$

#### 4.3. Sherwood number

The proportion of diffused mass transmission to convectional mass transmission is known as the Sherwood number. The rate of mass transmission (Sherwood number)  $Sh|_{\eta = -1}$  as well as  $Sh|_{\eta = 1}$  at the top and bottom surfaces of the surface contain the said mathematical equation,

$$Sh|_{\eta = -1} = \frac{kq_z}{(D_b)_{nf}(C_1 - C_2)} \Big|_{\eta = -1} = -\chi'(-1)$$

$$Sh|_{\eta = 1} = \frac{kq_z}{(D_b)_{nf}(C_1 - C_2)} \Big|_{\eta = 1} = -\chi'(1)$$

where

$$q_z|_{\eta = -1} = -\left( D_b \right)_{nf} \left( \frac{\partial C}{\partial z} \right) \Big|_{\eta = -1} = -\left( D_b \right)_{nf} \frac{(C_1 - C_2)}{k} \chi'(-1)$$

$$q_z|_{\eta = 1} = -\left( D_b \right)_{nf} \left( \frac{\partial C}{\partial z} \right) \Big|_{\eta = 1} = -\left( D_b \right)_{nf} \frac{(C_1 - C_2)}{k} \chi'(1)$$

### 5. Result and discussion

Using a shooting technique, the missing initial condition at the interval's starting position is assumed, and the ordinary differential equation is then numerically integrated as a boundary-value problem. The accuracy of the assumed missing initial condition is checked by comparing the computed value of the dependent variable at the output end with its given value. If there is a discrepancy, a different value is used. The initial conditions for the system of equations are

carefully selected to convert them into initial value problems, which are then solved using the 4th-order Runge-Kutta method. We have chosen the numerical initial values that satisfy the boundary requirements and provide an acceptable degree of accuracy. The shooting technique and the Runge-Kutta method are used for numerical calculations due to their low computing costs, minimal memory issues, and ability to produce precise and accurate results in a short amount of time. We have formulated a comprehensive system of nonlinear coupled ordinary differential equations that exhibit matrix composite material and hybrid nanofluid properties. The key advantage of this approach is its speed and adaptability to the problem of initial values. Although boundary value problems may be relatively stable, some initial value problems can be intrinsically unstable and have rising error modes beyond the shooting technique. The shooting technique is incredibly effective in locating initial value problems, which have many practical and real-world applications. In mathematical observation, the shooting approach is used to solve boundary value problems by reducing them to systems of initial value problems. We shoot out routes in different directions until we find a route that satisfies the necessary boundary value. The logical shooting method using ND solves in mathematics has been correctly employed for the nonlinear coupled Eq. (34). This section explains the effect of flow on several factors, including the expansion/contraction ratio factor ( $\alpha$ ), volume fraction ( $\phi$ ), magnetic field ( $M$ ), Brinkman numbers (Br), and the permeable Reynolds parameter (Re). Additionally, engineering parameters such as the coefficients of shear stress at both higher and lower walls, as well as the rates of heat and mass movement, are estimated computationally against the relevant factors. Table 1 presents the thermophysical properties of the nanoparticle and base fluid. We express confidence in our computational approach, as demonstrated in Table 2, wherein our numerical findings exhibit convergence with the reduction of the step size. Our boundary conditions are meticulously met, employing both symmetric configurations and accurate shear stress data at the bottom wall.

**Table 1.** Thermophysical properties of base fluid and nanoparticle.

Properties	$\rho$ (kg m <sup>-3</sup> )	$C_p$ (J kg <sup>-1</sup> K <sup>-1</sup> )	$K$ (W m <sup>-1</sup> K <sup>-1</sup> )
H <sub>2</sub> O (water)	997.1	4179	0.613
Au (gold)	19,300	129	318

**Table 2.** Numerical stability varies from -1 to 1.

$\eta$	$f(-1)$	$f'(-1)$	$f''(-1)$
-1	-1	0	2.8682185248890812
-0.9	-0.986004632148899	0.2762900573162856	2.6513635499005477
-0.8	-0.9455224728264963	0.5291984277529419	2.4022339523123413
-0.7	-0.8810372014384086	0.7559667541088714	2.129942115638948
-0.6	-0.7952655915371383	0.9546625435491819	1.8418610445096326
-0.5	-0.6910837969233515	1.1240010434185939	1.5435889317798919
-0.4	-0.5714712122097215	1.263175625521357	1.2391316972955884
-0.3	-0.4394701755700228	1.371712201118385	0.93118511715582
-0.2	-0.29815875720869417	1.4493534762608988	0.6214396059796121
-0.1	-0.1506336107568336	1.4959731677879262	0.31087067312291067
0	1.55484340680353 × 10 <sup>-10</sup>	1.5115177949361303	1.2913497632327 × 10 <sup>-9</sup>
0.1	0.1506336107568336	1.4959731683236508	0.31087067312291067
0.2	0.29815875720869417	1.4493534762608988	0.6214396059796121
0.3	0.4394701755700228	1.371712201118385	0.93118511715582
0.4	0.5714712122097215	1.263175625521357	1.2391316972955884
0.5	0.6910837969233515	1.1240010434185939	1.5435889317798919
0.6	0.7952655915371383	0.9546625435491819	1.8418610445096326
0.7	0.8810372014384086	0.7559667541088714	2.129942115638948
0.8	0.9455224728264963	0.5291984277529419	2.4022339523123413
0.9	0.986004632148899	0.2762900573162856	2.6513635499005477
1	1	0	2.8682185248890812

The physical parameters that directly relate to shear stress, heat, and mass at the bottom side-walls of porous media are shown by  $f''(-1)$ ,  $\chi'(-1)$ , and  $\theta'(-1)$ , respectively. The strong boundaries for the present study are the porous Reynolds numbers  $Re$ , the magnetic parameters  $M$ , the Brinkman numbers  $Br$ , the expansion/contraction ratios  $\alpha$ s, the Schmidt numbers  $Sc$ , the nanoparticle volume fractions parameters  $\phi$ , and the chemical reactions parameters  $C$ . Additionally, as in this literature, the evaluations associated with various boundaries have been treated as arbitrary. Further, the most ordinarily utilized reaches for these diverse non-dimensional boundaries are  $\phi = \{0.01, 0.02, 0.03, 0.04, 0.05, 0.06, 0.07, 0.08\}$ .  $M = \{1, 3, 5, 7, 9, 11, 13, 15, 16\}$ .  $Br = \{0.04, 0.06, 0.08, 0.10, 0.12, 0.14, 0.16, 0.18\}$ .  $\alpha = \{-1.5, -1, -0.5, 0, 0.5, 1, 1.5, 2\}$ .  $Re = \{-1.5, -1, -0.5, 0, 0.5, 1, 1.5, 2\}$ ,  $C = \{0.2, 0.4, 0.6, 0.8, 1.0, 1.2, 1.4, 1.6\}$   $h = \{0.01, 0.02, 0.03, 0.04, 0.05, 0.06, 0.07\}$  and  $r = \{0.5, 0.6, 0.7, 0.8, 0.9, 1\}$  are shown in [Tables 3](#) and [4](#). [Tables 3](#) and [4](#) depend on two cases varies of  $Re$  and  $\alpha$  form negative values to positive values check the effect of different nondimensional parameters on shear stress ( $f''(-1)$ ), the flow of heat transfer  $\theta'(-1)$  as well as mass transfer ( $\chi'(-1)$ ) of the lower porous wall. [Table 3](#) depicts the impact of the permeable Reynolds number ( $Re$ ) on the expansion ratio parameter ( $\alpha$ ) and volume fraction ( $\phi$ ). When  $Re$  is either less than 0 or greater than 0, there is an increase in the values of  $\alpha$  and  $\phi$ . This results in a decrease in the flow variables  $f''(-1)$ ,  $\chi'(-1)$ , and  $\theta'(-1)$ . However, the magnetic parameter ( $M$ ) values are greater than zero, leading to an elevation in the flow of shear stress ( $f''(-1)$ ). Furthermore, the augmentation of  $Br$ ,  $C$ , and  $h$  values enhances the flow of heat and mass transfer rate on the lower porous surface. Conversely, for cases where  $Re$  is less than zero, increasing the values of  $r$  diminishes the flow of thermal transfer on the lower porous surface. Additionally, on the bottom porous surface, elevating the values of  $Br$  and  $r$  increases the flow of heat and mass transfer rate. Yet, when  $h$  and  $C$  values are greater than zero, the flow of thermal and mass transfer rate is diminished in instances where  $Re$  is greater than 0. [Table 4](#) show the effect of expending/contracting parameter  $\alpha$  lies from  $-1$  to  $+1$  fixed values and many more parameter using different values check the effect of  $f''(-1)$ ,  $\chi'(-1)$  and  $\theta'(-1)$  and numerical results calculated. First of all, the values of permeable  $Re$ ,  $\phi$ , and  $M$  then the flow of  $f''(-1)$ ,  $\chi'(-1)$  and  $\theta'(-1)$  are enhanced in both cases  $\alpha$  values are  $-ve$  to  $+ve$  but  $Br$ ,  $h$ ,  $r$ , and  $C$  are greater than zero the flow of heat and mass transfer act opposite in lower porous walls. As a result, as shown in [Tables 3](#) and [4](#), we have numerically examined the effects of Reynolds number ( $Re$ ) and wall expansion ratio ( $\alpha$ ) on the real numbers at the wall of permeable channels impacted by chemical reactions. Shear stress increases during injection instances when  $Re < 0$  and  $\alpha < 0$  for metallic nanofluids (Au-water), whereas the mass transfer and heat transfer rates show various dimensional characteristics. Similarly, during attraction instances, shear stress diminishes, but the dimensional parameters of mass transfer and heat transfer rates alter entirely. For metallic nanofluids (Au-water), shear stress, heat transfer, and mass transfer rates increase under suction conditions when  $Re > 0$  and  $\alpha > 0$ , while during injection conditions, the converse is true.

The shear stress affects the mass of the channels for metallic nanofluids under the influence of the porous Reynolds numbers. During injection, the contrast between the shear stress  $f''(-1)$  and  $f''(1)$  of metals increases. Similar behavior is observed in withdrawal cases. There is a significant difference in the shear stresses for metallic nanofluids (Au-water) under withdrawal scenarios compared to the relaxation of the permeable walls. When the expansion ratio parameter  $\alpha$  is positive and the Reynolds number varies from negative to positive, the flow of shear stress decreases. However, when the expansion ratio  $\alpha$  is positive, the flow of shear stress increases, as shown in [Figure 4\(A\)](#) and [\(B\)](#). [Figure 5](#) illustrates the physical significance of the expansion ratio parameter as it shifts from negative to positive values in radial velocity profile. The plot shows that the thickness of the momentum boundary layer at the middle of the wall increases when the expansion ratio is positive, while it reduces on both porous surfaces. This finding implies that the

**Table 3.** Effects of Re on shear stress, heat transfer, and mass transfer are investigated when Re varies from -0.5 to 0.5.

Re	$\alpha$	$\phi$	M	Br	C	H	r	$f'(-1)$	$ \theta'(-1) $	$ \chi'(-1) $						
-0.5	-1.5	0.02	1	0	0	0.01	0.5	5.0912	1.9360	0.5611						
	-1							4.4117	0.9948	0.4730						
	-0.5							3.7629	0.4247	0.3963						
	0							3.1497	0.1551	0.3299						
	0.5							2.5765	0.0508	0.2729						
	1							2.0479	0.0155	0.2246						
	1.5							1.5678	0.0045	0.1838						
	2							1.1393	0.00128	0.1496						
	1							0.01 = 1%	1	0	0	0.01	0.5	2.2541	0.0142	0.2253
								0.02 = 2%						2.0479	0.0226	0.2246
		0.03 = 3%	1.8226	0.0333	0.2237											
		0.04 = 4%	1.5849	0.0465	0.2227											
		0.05 = 5%	1.3483	0.0619	0.2214											
		0.06 = 6%	1.1338	0.0794	0.2201											
		0.07 = 7%	0.96606	0.0988	0.2186											
		0.08 = 8%	0.8600	0.1199	0.2172											
		0.02	1	0	0	0.01	0.5	2.0479	0.0155	0.2246						
								3	2.4741	0.0155	0.2246					
								5	2.8585	0.0155	0.2246					
								7	3.2101	0.0155	0.2246					
								9	3.5350	0.0155	0.2246					
								11	3.8382	0.0155	0.2246					
								13	4.1229	0.0155	0.2246					
			15	4.3922	0.0155	0.2246										
		0.02	1	0.04	0	0.01	0.5	2.0479	0.0182	0.2246						
								0.06	2.0479	0.0161	0.2246					
								0.08	2.0479	0.0139	0.2246					
								0.10	2.0479	0.0118	0.2246					
								0.12	2.0479	0.0096	0.2246					
								0.14	2.0479	0.0074	0.2246					
								0.16	2.0479	0.0053	0.2246					
								0.18	2.0479	0.0031	0.2246					
		0.2						2.0479	0.0155	0.3021						
		0.4						2.0479	0.0155	0.3742						
		0.6	2.0479	0.0155	0.4428											
		0.8	2.0479	0.0155	0.5082											
		1.0	2.0479	0.0155	0.5707											
		1.2	2.0479	0.0155	0.6306											
		1.4	2.0479	0.0155	0.6883											
		1.6	2.0479	0.0155	0.7442											
				0.02	2.0479	0.3355	0.2246									
				0.03	2.0479	0.3765	0.2246									
				0.04	2.0479	0.3920	0.2246									
				0.05	2.0479	0.4520	0.2246									
				0.06	2.0479	0.48790	0.2246									
				0.07	2.0479	0.5787	0.2246									
				0.6	2.0479	0.3139	0.2246									
				0.7	2.0479	0.3118	0.2246									
				0.8	2.0479	0.3099	0.2246									
				0.9	2.0479	0.3082	0.2246									
				1	2.0479	0.3070	0.2246									
0.5	-1.5	0.02	1	0	0			5.7149	4.2076	1.1071						
	-1							4.9125	3.0466	0.9686						
	-0.5							4.1247	1.9986	0.8429						
	0							3.3545	1.1587	0.7329						
	0.5							2.6068	0.5883	0.6293						
	1							1.8847	0.2652	0.5402						
	1.5							1.1928	0.1091	0.4621						
	2							0.5345	0.0423	0.3940						
	1							0.01 = 1%	1	0	0	0.01	0.5	2.1924	0.2396	0.5384
								0.02 = 2%						1.8847	0.2652	0.5402
		0.03 = 3%	1.4713	0.2899	0.5429											
		0.04 = 4%	0.8815	0.3145	0.5471											

(continued)

**Table 3.** Continued.

Re	$\alpha$	$\phi$	$M$	Br	$C$	$H$	$r$	$\theta'(-1)$	$ \theta'(-1) $	$ \chi'(-1) $
		0.05 = 5%						0.4319	0.3406	0.5545
		0.06 = 6%						0.1167	0.3771	0.5639
		0.07 = 7%						0.0672	0.4070	0.5730
		0.08 = 8%						0.0298	0.4423	0.5771
	1	0.02	1	0	0	0.01	0.5	1.8847	0.2652	0.5402
			3					2.4663	0.2605	0.5369
			5					2.9610	0.2568	0.5342
			7					3.3944	0.2539	0.5321
			9					3.7825	0.2514	0.5304
			11					4.1355	0.2493	0.5289
			13					4.4610	0.2476	0.5276
			15					4.7639	0.2461	0.5265
	1	0.02	1	0.04	0	0.01	0.5	1.8874	0.2534	0.5402
				0.06				1.8875	0.2475	0.5402
				0.08				1.8875	0.2415	0.5402
				0.10				1.8874	0.2357	0.5402
				0.12				1.8875	0.2298	0.5402
				0.14				1.8874	0.2238	0.5402
				0.16				1.8875	0.2179	0.5402
				0.18				1.8874	0.2120	0.5402
	1	0.02	1	0	0.2	0.01		2.1924	0.2396	0.6715
					0.4			1.8847	0.2653	0.7938
					0.6			1.4713	0.2899	0.9070
					0.8			0.8815	0.3023	1.0137
					1.0			0.4613	0.3145	1.1181
					1.2			0.0672	0.3406	1.1855
					1.4			0.0273	0.3570	1.2341
					1.6		0.5	0.0128	0.3772	1.2462
						0.02		1.8874	0.2264	0.5402
						0.03		1.8875	0.2750	0.5402
						0.04		1.8875	0.3419	0.5402
						0.05		1.8874	0.4035	0.5402
						0.06		1.8875	0.4540	0.5402
						0.07		1.8874	0.5147	0.5402
							0.6	1.8874	0.2139	0.5402
							0.7	1.8875	0.2118	0.5402
							0.8	1.8875	0.2099	0.5402
							0.9	1.8874	0.2082	0.5402
							1	1.8875	0.2070	0.5402

expansion ratio plays a critical role in determining the boundary layer thickness and, thus, the overall flow behavior in the permeable channels (Figure 6).

Figure 7 depicts the significant effects of the Brinkman number Br on the heat transfer in the permeable channels. The plot reveals that the thickness of the thermal boundary layer increase at the lower porous surface but increases in the middle of the walls as the Brinkman number values increases then the flow of heat transfer rate are reduced in upper porous disk. In contrast, the temperature profile are decreases in the middle of the upper porous walls but increases at the lower plates of the boundary layer.

Figure 8 shows the remarkable influence of the magnetic parameter  $M$  on the radial velocity profile in the permeable channels. The plot reveals that increasing the value of  $M$  from 1 to 15 has a significant impact on the thickness of the boundary layer at the top and bottom surfaces, which increases while decreases around the channel's midpoint. This finding underscores the crucial role played by the magnetic field in shaping the flow behavior in permeable channels and its potential applications in various fields such as engineering, physics, and material science.

Figure 9 presents a graphical representation of the thickness of the boundary layer as a function of the Reynolds number Re, based on the temperature profile in the permeable channels.

**Table 4.** Effects of  $\alpha$  on shear stress, heat transfer, and mass transfer are investigated when  $\alpha$  varies from  $-1$  to  $1$ .

$\alpha$	Re	$\phi$	M	Br	C	h	r	$f''(-1)$	$ \theta'(-1) $	$ \chi'(-1) $			
-1	-1.5	0.02	1	0	0	0.01	0.5	4.0332	0.1266	0.2005			
	-1							4.2089	0.3771	0.3129			
	-0.5							4.4116	0.9343	0.4730			
	0							4.6449	1.8625	0.6898			
	0.5							4.9124	3.0466	0.9686			
	1							5.2180	4.3204	1.3086			
	1.5							5.5649	5.5954	1.7036			
	2							5.9562	6.8501	2.1430			
	-0.5							0.01 = 1%	1	0	0	0.01	0.5
		0.02 = 2%	4.4116	0.9343	0.4730								
		0.03 = 3%	4.7560	0.8759	0.4742								
		0.04 = 4%	5.1829	0.8275	0.4755								
		0.05 = 5%	5.7223	0.7870	0.4770								
		0.06 = 6%	6.4210	0.7527	0.4788								
		0.07 = 7%	6.7561	0.7271	0.4827								
		0.08 = 8%	7.1294	0.6956	0.4830								
	-0.5	0.02	1	0	0	0.01	0.5	4.4117					
			3					4.7763	0.9389	0.4742			
			5					5.1118	0.9429	0.4752			
			7					5.4235	0.9463	0.4763			
			9					5.7156	0.9494	0.4771			
			11					5.9910	0.9521	0.4779			
			13					6.2521	0.9546	0.4785			
		15	6.5007	0.9568	0.4791								
	-0.5	0.02	1	0.04	0	0	0.01	0.5	4.4117	0.9077	0.47404		
				0.06					4.4116	0.8944	0.47404		
				0.08					4.4117	0.8810	0.47404		
				0.10					4.4116	0.8677	0.47404		
	0.12			4.4117					0.8543	0.47404			
	0.14			4.4116					0.8409	0.47404			
	0.16			4.4117					0.8277	0.47404			
	0.18			4.4116					0.8143	0.47404			
-0.5	0.02			1					0	0.2	0	0.01	0.5
		0.4	4.4116		0.9343	0.7071							
		0.6	4.7560		0.8759	0.8119							
		0.8	5.1829		0.8275	0.9098							
		1.0	5.4655		0.7870	1.0020							
		1.2	5.7223		0.7525	1.0894							
		1.4	6.4215		0.7122	1.2071							
		1.6	6.6294		0.6759	1.3583							
						0.02	4.4116	0.1530		0.47404			
						0.03	4.4117	0.2451		0.47404			
						0.04	4.4116	0.2954		0.47404			
						0.05	4.4117	0.3279		0.47404			
						0.06	4.4116	0.3515		0.47404			
						0.07	4.4117	0.3987		0.47404			
						0.6	4.4116	0.0187		0.47404			
						0.7	4.1294	0.0175		0.47404			
						0.8	4.4116	0.0164		0.47404			
				0.9	4.4116	0.0152	0.47404						
				1	4.4117	0.0144	0.47404						
1	-1.5	0.02	1	0	0	0.01	0.5	2.1482	0.00069	0.0828			
	-1							2.1037	0.0034	0.1381			
	-0.5							2.0479	0.0155	0.2246			
	0							1.9768	0.0663	0.3544			
	0.5							1.8847	0.2469	0.5402			
	1							1.7636	0.7329	0.7918			
	1.5							1.6010	1.6344	1.1130			
	2							1.3787	2.8268	1.5003			
	-0.5							0.01 = 1%	1	0	0	0.01	0.5
		0.02 = 2%	2.0479	0.0226	0.2246								
		0.03 = 3%	1.8226	0.0333	0.2237								
		0.04 = 4%	1.5849	0.0465	0.2227								

(continued)

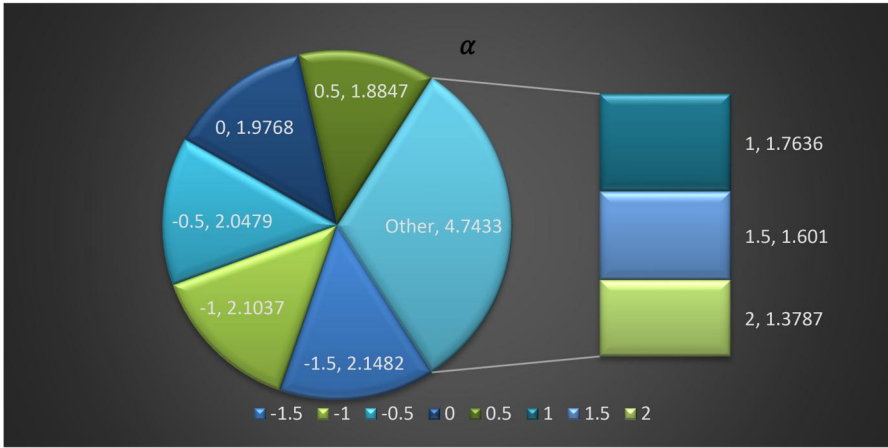
**Table 4.** Continued.

$\alpha$	Re	$\phi$	$M$	Br	$C$	$h$	$r$	$f''(-1)$	$ \theta'(-1) $	$ \chi'(-1) $
		0.05 = 5%						1.3483	0.0619	0.2214
		0.06 = 6%						1.1338	0.0794	0.2201
		0.07 = 7%						0.96606	0.0988	0.2186
		0.08 = 8%						0.8600	0.1199	0.2172
	-0.5	0.02	1	0	0	0.01	0.5	2.0479	0.0155	0.2246
			3					2.4741	0.0158	0.2259
			5					2.8585	0.0161	0.2272
			7					3.2101	0.0164	0.2282
			9					3.5350	0.0166	0.2290
			11					3.8382	0.0168	0.2298
			13					4.1229	0.0169	0.2305
			15					4.3922	0.0171	0.2311
	-0.5	0.02	1	0.04	0	0.01	0.5	2.0479	0.0182	0.2246
				0.06				2.0479	0.0161	0.2246
				0.08				2.0479	0.0139	0.2246
				0.10				2.0479	0.0118	0.2246
				0.12				2.0479	0.0096	0.2246
				0.14				2.0479	0.0074	0.2246
				0.16				2.0479	0.0053	0.2246
				0.18				2.0479	0.0031	0.2247
	-0.5	0.02	1	0	0.2			2.2541	0.0142	0.3021
					0.4			2.2541	0.0142	0.3742
					0.6			2.2541	0.0142	0.4428
					0.8			2.2541	0.0142	0.5082
					1.0			2.2541	0.0142	0.5707
					1.2			2.2541	0.0142	0.6306
					1.4			2.2541	0.0142	0.6883
					1.6			2.2541	0.0142	0.2246
						0.02		2.0479	0.0620	0.2246
						0.03		2.0479	0.1336	0.2246
						0.04		2.0479	0.2054	0.2246
						0.05		2.0479	0.2179	0.2246
						0.06		2.0479	0.2241	0.2246
						0.07		2.0479	0.2278	0.2246
							0.6	2.0479	0.0078	0.2247
							0.7	2.0479	0.0067	0.2246
							0.8	2.0479	0.0050	0.2246
							0.9	2.0479	0.0041	0.2246
							1	2.0479	0.0034	0.2246

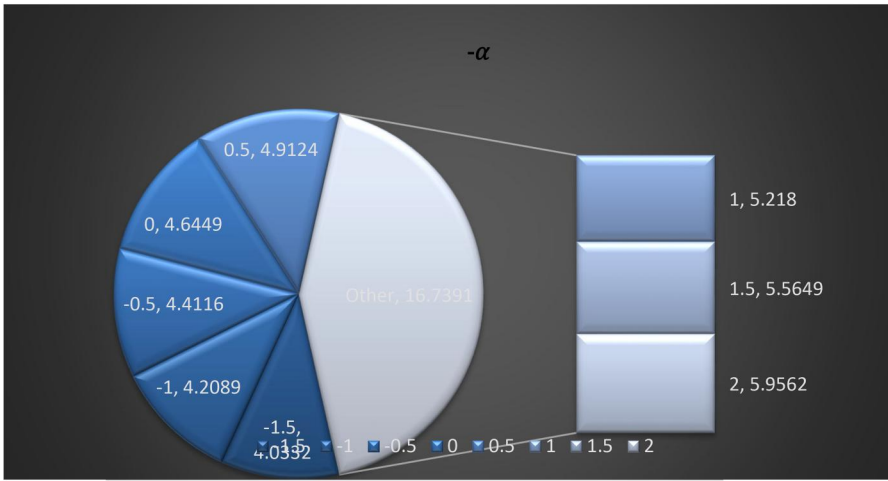
The boundary layer refers to the region adjacent to the solid surface where the velocity of the fluid changes rapidly from zero to the free stream velocity. The thickness of this boundary layer plays a significant role in the overall heat and mass transfer rates in the permeable channels. The results in [Figure 9](#) demonstrate that an increase in the Reynolds number from  $-1.5$  to  $2$  causes the thickness of the boundary layer to decrease for the lower layers, while it increases for the upper layer.

[Figure 10](#) presents a graphical representation of the effect of the volume fraction  $\phi$  on the temperature profile in the permeable channels. The volume fraction refers to the ratio of the volume of the nanoparticles to the volume of the base fluid in the nanofluid. Specifically, when the volume fraction increases from  $0.01$  to  $0.08$ , the thickness of the boundary layer decreases for the upper plate and increases for the lower plate. This finding highlights the importance of considering the volume fraction in the design and analysis of nanofluid-based permeable channel systems.

[Figure 11](#) illustrates the effects of chemical reaction parameter  $C$ , which consists of concentration profile. The thickness of the boundary layer on the flow mass transfer decreases at the lower and upper plates in the concentration profile.



(A)



(B)

**Figure 4.** (A) Effect of sRe on shears stress for metallics particles when  $\alpha > 0$ . (B) Effect of sRe on shears stress for metallics particles when  $\alpha < 0$ .

## 6. Conclusions

The simulation calculations for the nanoparticles demonstrate the impact of the chemical process on the transition temperature of the viscous dissipative flow of nanofluid, as well as the MHD impact through a porous medium (gold). The effect of the controlling parameters on the problem's momentum, mass transfer, and heat transfer characteristics has been investigated. These parameters include the Reynolds number, magnetic factor, Schmidt number, Brinkman number, wall expansion/contraction ratio, nanoparticle volume fraction, and chemical reaction parameter. The study's findings can be used to derive the following statements:

If there should be an occurrence of moving toward dividers, the shear stress flow of heat transfer as well as mass transmission rates (for the Au nanofluid) at the channel dividers increase for injection, though a contrary impact is seen for suction.

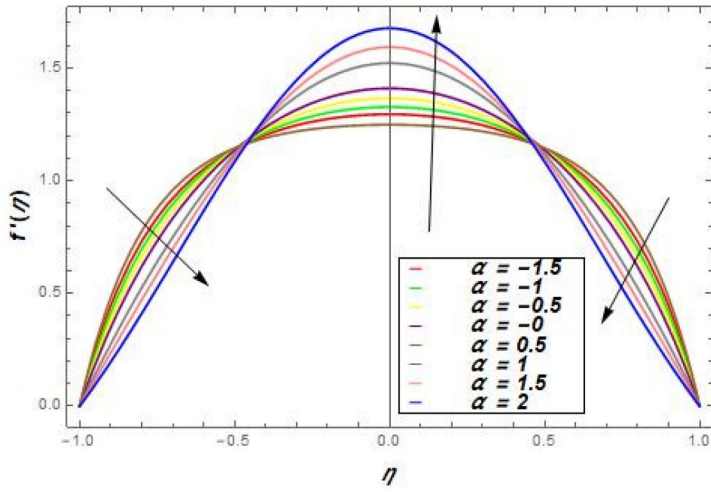
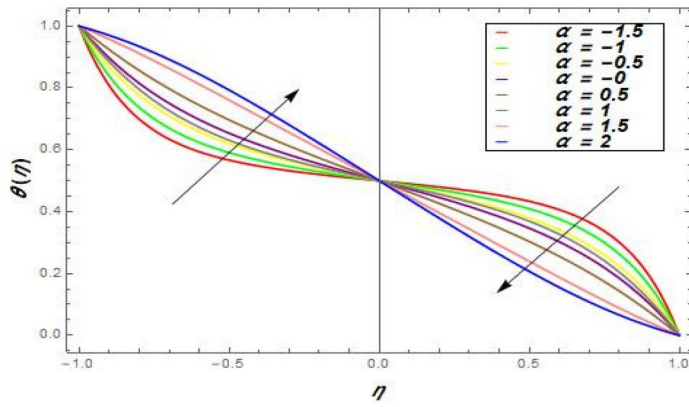
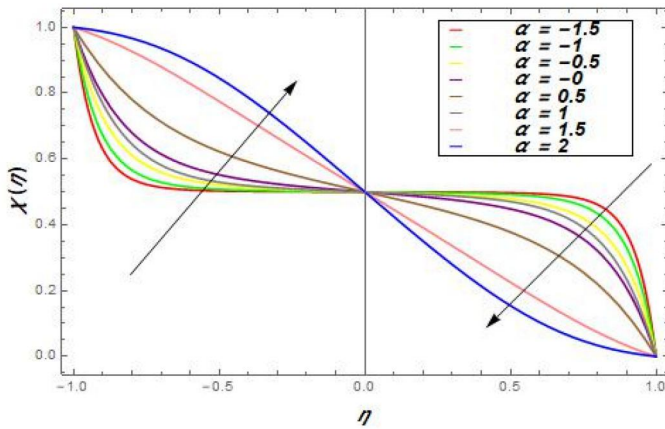


Figure 5. Radial velocity profile for  $Re = -0.5, Pr = 6.2, Br = 0, sc = 1, \phi = 0.02, M = 1, Tr = 0, C = 0$ .



(a)



(b)

Figure 6. (a, b) Simultaneous the temperature and concentration profile for  $Br = 0, Re = -0.5, Pr = 6.2, sc = 1, \phi = 0.02, M = 1, Tr = 0, C = 0$ .

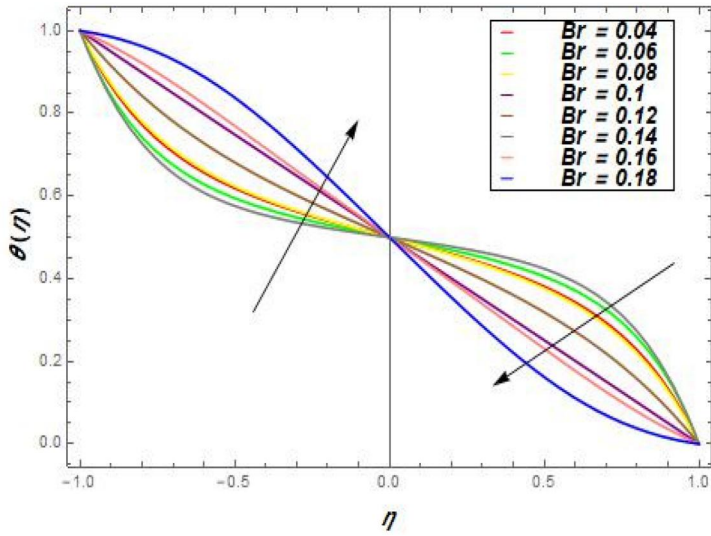


Figure 7. Temperature profile for  $\alpha = 1, Re = -0.5, Pr = 6.2, C = 0, Sc = 1, \phi = 0.02, M = 1, Tr = 0$ .

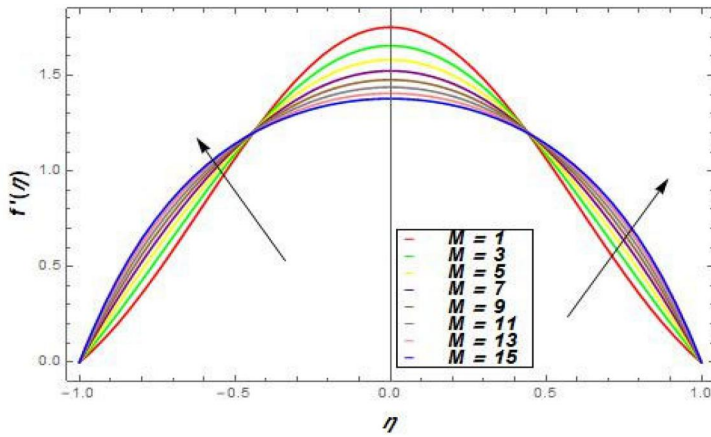


Figure 8. Radial velocity profile for  $\alpha = 1, Re = 0.5, Pr = 6.2, Br = 0, sc = 1, Tr = 0, C = 0$ .

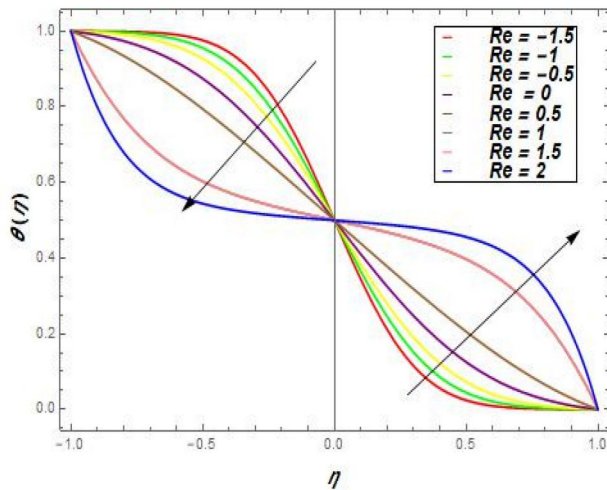


Figure 9. Temperature profile for  $\alpha = 1, Re = 0.5, Pr = 6.2, Br = 0, Sc = 1, M = 1$ .

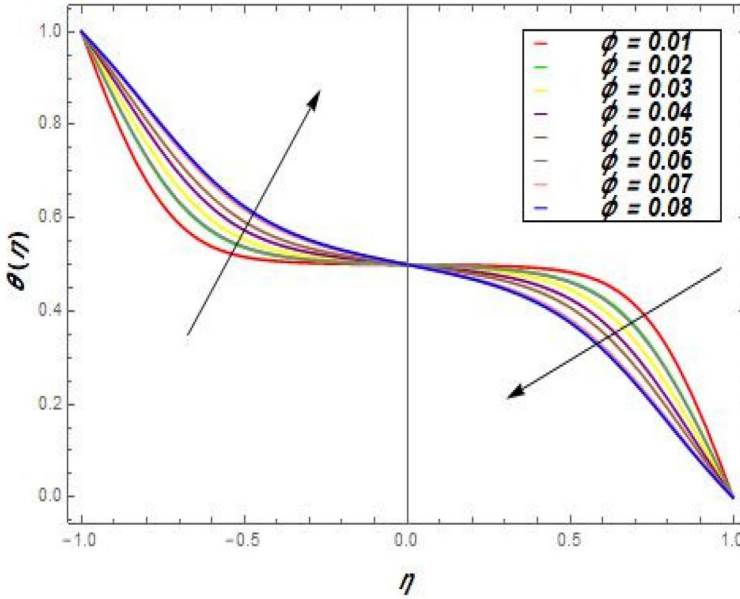


Figure 10. Temperature profile for  $\alpha = -1, \text{Re} = -0.5, \text{Pr} = 6.2, \text{Br} = 0, \text{sc} = 1, M = 1, \text{Tr} = 0, C = 0$ .

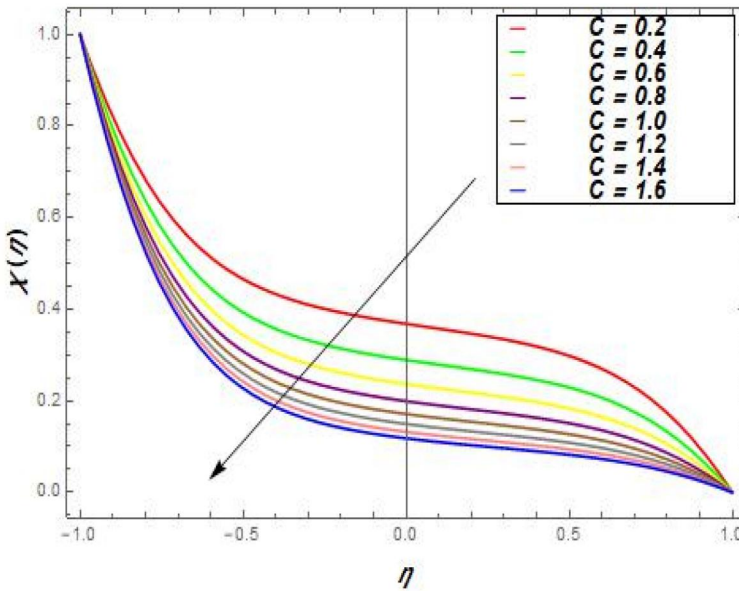


Figure 11. Concentration profile for  $\alpha = -1, \text{Re} = 0.5, \text{Pr} = 6.2, \text{sc} = 1$ .

- When the Br number is increased and the expansion ratio and Reynolds number are held constant within a range of negative to positive values, the flow of heat transfer is reduced in the lower wall.
- Increasing the values of magnetic field and chemical reaction parameters  $C$  enhances the flow of momentum and concentration boundary layer on both porous walls.
- The flow of shear stress, heat transfer, and mass transfer in the lower porous surface is enhanced by increasing the values of the Reynolds number and volume fraction for expansion ratio parameter constant values of  $-1$  to  $1$  in both cases.

- Rise the values of the expansion ratio parameter then the flow of thermal, momentum and mass transfer gradually increase.
- The thermal conductivity of nanolayer values is increased and the flow of thermal transfer is enhanced.
- The radius of nanoparticles  $r$  is greater than zero flow of thermal conductivity layer is reduced in the lower porous surface.

## Funding

The authors extend their appreciation to the Deputyship for Research & Innovation, Ministry of Education in Saudi Arabia for funding this research work through the project number ISP23-66 and this work is supported by the Fundamental Research Funds for the Central Universities (Grant No. D5000230061).

## Disclosure Statement

No potential conflict of interest was reported by the author(s).

## ORCID

Qadeer Raza  <http://orcid.org/0009-0008-4831-5606>

Ali J. Chamkha  <http://orcid.org/0000-0002-8335-3121>

## References

- [1] A. Diachenko, "Fractal models," *Archaeol. Sci.*, vol. 11, pp. 1–4, 2018. DOI: [10.1002/9781119188230.saseas0248](https://doi.org/10.1002/9781119188230.saseas0248).
- [2] J. Cai, E. Perfect, C. L. Cheng, and X. Hu, "Generalized modeling of spontaneous imbibition based on Hagen–Poiseuille flow in tortuous capillaries with variably shaped apertures," *Langmuir*, vol. 30, no. 18, pp. 5142–5151, 2014. DOI: [10.1021/la5007204](https://doi.org/10.1021/la5007204).
- [3] X. Yang, Y. Liang, and W. Chen, "A fractal roughness model for the transport of fractional non-Newtonian fluid in microtubes," *Chaos Solitons Fractals*, vol. 126, pp. 236–241, 2019. DOI: [10.1016/j.chaos.2020.109812](https://doi.org/10.1016/j.chaos.2020.109812).
- [4] J. Cai, X. Hu, B. Xiao, Y. Zhou, and W. Wei, "Recent developments on fractal-based approaches to nanofluids and nanoparticle aggregation," *Int. Commun. Heat Mass Transf.*, vol. 105, pp. 623–637, 2017. DOI: [10.1016/j.ijheatmasstransfer.2016.10.011](https://doi.org/10.1016/j.ijheatmasstransfer.2016.10.011).
- [5] Y. Li, *et al.*, "Semi-analytical correlation for pool boiling heat transfer using nanofluids based on fractal theory," *IOP Conf. Ser.: Mater. Sci. Eng.*, vol. 774, no. 1, pp. 012061, 2020. DOI: [10.1088/1757-899X/774/1/012061](https://doi.org/10.1088/1757-899X/774/1/012061).
- [6] Y. Shi, M. R. Yassin, and H. Dehghanpour, "A modified model for spontaneous imbibition of wetting phase into fractal porous media," *Colloids Surf. A Physicochem. Eng.*, vol. 543, pp. 64–75, 2018. DOI: [10.1016/j.colsurfa.2017.12.052](https://doi.org/10.1016/j.colsurfa.2017.12.052).
- [7] T. Miao, A. Chen, Y. Xu, S. Cheng and K. Wang, "A permeability model for water–gas phase flow in fractal fracture networks," *Fractals*, vol. 26, no. 06, pp. 1850087, 2018. DOI: [10.1142/S0218348X18500871](https://doi.org/10.1142/S0218348X18500871).
- [8] P. Xu, *et al.*, "Effective permeability of fractured porous media with fractal dual-porosity model," *Fractals*, vol. 25, no. 04, pp. 1740014, 2017. DOI: [10.1166/jnn.2017.14502](https://doi.org/10.1166/jnn.2017.14502).
- [9] M. Z. Qureshi, *et al.*, "Fractal flow model for cluster interfacial nanolayer of magnetized metallic oxides nanomaterials," *Int. Commun. Heat Mass Transf.*, vol. 139, no. 1, pp. 106419, 2022. DOI: [10.1016/j.icheatmasstransfer.2022.106419](https://doi.org/10.1016/j.icheatmasstransfer.2022.106419).
- [10] S. Yan and Y. Liang, "A space fractal derivative temperature model in characterization of chloride ions super diffusion in concrete in a marine environment," *J. Building Eng.*, vol. 78, no. 1, pp. 107669, 2023. DOI: [10.1016/j.jobe.2023.107669](https://doi.org/10.1016/j.jobe.2023.107669).
- [11] Y. Liang, N. Su, and W. Chen, "A time-space Hausdorff derivative model for anomalous transport in porous media," *FCAA*, vol. 22, no. 6, pp. 1517–1536, 2019. DOI: [10.1515/fca-2019-0079](https://doi.org/10.1515/fca-2019-0079).
- [12] Y. Liang, W. Chen, and W. Cai, *Hausdorff Calculus: Applications to Fractal Systems*. Walter de Gruyter GmbH & Co KG, 2019.

- [13] J. Chen, D. Han, S. Gao, W. He, and T. Peng, "Use of single air extraction and injection to thermodynamically balance the combined heat and mass transfer process," *Energy*, vol. 224, pp. 120193–124, 2021. DOI: [10.1016/j.energy.2021.120193](https://doi.org/10.1016/j.energy.2021.120193).
- [14] S. Poddar, M. M. Islam, J. Ferdouse and M. M. Alam, "Characteristic analysis of MHD heat and mass transfer dissipative and radiating fluid flow with magnetic field induction and suction," *SN Appl. Sci.*, vol. 3, no. 4, pp. 1–17, 2021. DOI: [10.1007/s42452-021-04452-4](https://doi.org/10.1007/s42452-021-04452-4).
- [15] M. Narahari and B. K. Dutta, "Effects of mass transfer and free-convection currents on the flow near a moving vertical plate with ramped wall temperature," *Heat Transf. Summer Conf.*, vol. 43574, pp. 63–72, 2009. DOI: [10.1115/HT2009-88045](https://doi.org/10.1115/HT2009-88045).
- [16] M. O. Allah, "Viscous potential flow analysis of interfacial stability with mass transfer through porous media," *Appl. Math. Comput.*, vol. 217, no. 20, pp. 7920–793, 2011. DOI: [10.1016/j.amc.2011.02.066](https://doi.org/10.1016/j.amc.2011.02.066).
- [17] A. T. J. Finkler, *et al.*, "Estimation of heat and mass transfer coefficients in a pilot packed-bed solid-state fermentation bioreactor," *Chem. Eng. J.*, vol. 408, pp. 127246, 2021. DOI: [10.1016/j.cej.2020.127246](https://doi.org/10.1016/j.cej.2020.127246).
- [18] P. S. Reddy and P. Sreedevi, "Effect of zero mass flux condition on heat and mass transfer analysis of nanofluid flow inside a cavity with magnetic field," *Eur. Phys. J. Plus*, vol. 136, no. 1, pp. 1–24, 2021. DOI: [10.1140/epjp/s13360-021-01095-7](https://doi.org/10.1140/epjp/s13360-021-01095-7).
- [19] N. A. Shah, S. Wang, T. Elnaqeeb, and H. Qi, "Soret and memory effects on unsteady MHD natural convection heat and mass transfer flow in a porous medium with Newtonian heating," *J Por Media*, vol. 24, no. 7, pp. 45–59, 2021. DOI: [10.1615/JPorMedia.2021026614](https://doi.org/10.1615/JPorMedia.2021026614).
- [20] Y. Mao, J. Robinson, and E. Binner, "Understanding heat and mass transfer processes during microwave-assisted and conventional solvent extraction," *Chem. Eng. Sci.*, vol. 233, pp. 116418, 2021. DOI: [10.1016/j.ces.2020.116418](https://doi.org/10.1016/j.ces.2020.116418).
- [21] G. V. Kuznetsov, *et al.*, "Features of the processes of heat and mass transfer when drying a large thickness layer of wood biomass," *Renew. Energy*, vol. 169, pp. 498–511, 2021. DOI: [10.1016/j.renene.2020.12.137](https://doi.org/10.1016/j.renene.2020.12.137).
- [22] X. Chen, S. Du, R. Z. Wang, and P. Lin, "Experimental study of heat and mass transfer for ammonia-water falling film absorption on novel S-shaped capillary tubes bundle," *Int. Commun. Heat Mass Transf.*, vol. 164, pp. 120606, 2021. DOI: [10.1016/j.ijheatmasstransfer.2020.120606](https://doi.org/10.1016/j.ijheatmasstransfer.2020.120606).
- [23] L. Abdelkrim and D. Mahfoud, "Heat and mass transfer in an inclined bi-L-shaped layered porous media: effect of buoyancy ration," *DDF*, vol. 406, pp. 87–97, 2021. DOI: [10.4028/www.scientific.net/DDF.406.87](https://doi.org/10.4028/www.scientific.net/DDF.406.87).
- [24] W. Gao, K. Xu, L. Ji, and B. Tang, "Effect of gold nanoparticles on glutathione depletion-induced hydrogen peroxide generation and apoptosis in HL7702 cells," *Toxicol. Lett.*, vol. 205, no. 1, pp. 86–95, 2011. DOI: [10.1016/j.toxlet.2011.05.1018](https://doi.org/10.1016/j.toxlet.2011.05.1018).
- [25] Z. Shen, L. Su, X. C. Yuan, and Y. C. Shen, "Trapping and rotating of a metallic particle trimer with optical vortex," *Appl. Phys. Lett.*, vol. 109, no. 24, pp. 241901, 2016. DOI: [10.1063/1.4971981](https://doi.org/10.1063/1.4971981).
- [26] M. V. S. Rao, K. Gangadhar, A. J. Chamkha, and P. Surekha, "Bioconvection in a convectational nanofluid flow containing gyrotactic microorganisms over an isothermal vertical cone embedded in a porous surface with chemical reactive species," *Arab. J. Sci. Eng.*, vol. 46, no. 3, pp. 2493–2503, 2021. DOI: [10.1007/s13369-020-05132-y](https://doi.org/10.1007/s13369-020-05132-y).
- [27] F. Saidoune, M. N. Bouaziz, and A. Aziz, "Conjugate heat and mass transfer on steady MHD mixed convection flow along a vertical slender hollow cylinder with heat generation and chemical reaction effects," *DDF*, vol. 406, pp. 53–65, 2021. DOI: [10.4028/www.scientific.net/DDF.406.53](https://doi.org/10.4028/www.scientific.net/DDF.406.53).
- [28] D. Gopal, *et al.*, "Numerical analysis of higher order chemical reaction on electrically MHD nanofluid under influence of viscous dissipation," *Alex. Eng. J.*, vol. 60, no. 1, pp. 1861–1871, 2021. DOI: [10.1016/j.aej.2020.11.034](https://doi.org/10.1016/j.aej.2020.11.034).
- [29] A. V. Minakov, D. V. Guzei, K. N. Meshkov, I. A. Popov, and A. V. Shchelchkov, "Experimental study of turbulent forced convection of nanofluid in channels with cylindrical and spherical hollows," *Int. Commun. Heat Mass Transf.*, vol. 115, pp. 915–925, 2017. DOI: [10.1016/j.ijheatmasstransfer.2017.07.117](https://doi.org/10.1016/j.ijheatmasstransfer.2017.07.117).
- [30] R. Mohebbi, M. M. Rashidi, M. Izadi, N. A. C. Sidik, and H. W. Xian, "Forced convection of nanofluids in an extended surfaces channel using lattice Boltzmann method," *Int. Commun. Heat Mass Transf.*, vol. 117, pp. 1291–1303, 2018. DOI: [10.1016/j.ijheatmasstransfer.2017.10.063](https://doi.org/10.1016/j.ijheatmasstransfer.2017.10.063).
- [31] R. Dormohammadi, M. Farzaneh-Gord, A. Ebrahimi-Moghadam, and M. H. Ahmadi, "Heat transfer and entropy generation of the nanofluid flow inside sinusoidal wavy channels," *J. Mol. Liq.*, vol. 269, pp. 229–240, 2018. DOI: [10.1016/j.molliq.2018.07.119](https://doi.org/10.1016/j.molliq.2018.07.119).
- [32] A. Wakif, Z. Boulahia, F. Ali, M. R. Eid, and R. Sehaqui, "Numerical analysis of the unsteady natural convection MHD Couette nanofluid flow in the presence of thermal radiation using single and two-phase nanofluid models for Cu-water nanofluids," *Int. J. Appl. Comput. Math.*, vol. 4, no. 3, pp. 81, 2018. DOI: [10.1007/s40819-018-0513-y](https://doi.org/10.1007/s40819-018-0513-y).
- [33] M. Sheikholeslami, M. Jafaryar and Z. Li, "Nanofluid turbulent convective flow in a circular duct with helical turbulators considering Cu nanoparticles," *Int. J. Heat Mass Transf.*, vol. 124, pp. 980–989, 2018. DOI: [10.1016/j.ijheatmasstransfer.2018.04.022](https://doi.org/10.1016/j.ijheatmasstransfer.2018.04.022).

- [34] T. Hayat, M. I. Khan, M. Waqas, A. Alsaedi and M. I. Khan, "Radiative flow of micropolar nanofluid accounting thermophoresis and Brownian moment," *Int. J. Hydrog. Energy*, vol. 42, no. 26, pp. 16821–16833, 2017. DOI: [10.1016/j.ijhydene.2017.05.006](https://doi.org/10.1016/j.ijhydene.2017.05.006).
- [35] G. Liang and I. Mudawar, "Review of pool boiling enhancement with additives and nanofluids," *Int. J. Heat Mass Transf.*, vol. 124, pp. 423–453, 2018. DOI: [10.1016/j.ijheatmasstransfer.2018.03.046](https://doi.org/10.1016/j.ijheatmasstransfer.2018.03.046).
- [36] S. Hussain, Z. Abbas, J. Hasnain, M. S. Arslan and A. Ali, "Thermally developed unsteady viscous nanofluid flow due to permeable channel with orthogonal motion of walls using Beavers-Joseph slip condition," *Alex. Eng. J.*, vol. 60, no. 2, pp. 2335–2345, 2021. DOI: [10.1016/j.aej.2020.12.043](https://doi.org/10.1016/j.aej.2020.12.043).
- [37] Z. Nisar, T. Hayat, A. Alsaedi, and B. Ahmad, "Wall properties and convective conditions in MHD radiative peristalsis flow of Eyring–Powell nanofluid," *J. Therm. Anal. Calorim.*, vol. 144, no. 4, pp. 1199–1208, 2021. DOI: [10.1007/s10973-020-09576-0](https://doi.org/10.1007/s10973-020-09576-0).
- [38] R. P. Gowda, "Computational modeling of nanofluid flow over a curved stretching sheet using Koo–Kleinstreuer and Li (KKL) correlation and modified Fourier heat flux model," *Chaos, Solitons Fractals*, vol. 145, pp. 110774, 2021. DOI: [10.1016/j.chaos.2021.110774](https://doi.org/10.1016/j.chaos.2021.110774).
- [39] A. A. Arafa, Z. Z. Rashed, and S. E. Ahmed, "Radiative MHD bioconvective nanofluid flow due to gyrotactic microorganisms using Atangana–Baleanu Caputo fractional derivative," *Phys. Scr.*, vol. 96, no. 5, pp. 055211, 2021. DOI: [10.1088/1402-4896/abe82d](https://doi.org/10.1088/1402-4896/abe82d).
- [40] S. K. Das, N. Putra, P. Thiesen, and W. Roetzel, "Temperature dependence of thermal conductivity enhancement for nanofluids," *J. Heat Transf.*, vol. 125, no. 4, pp. 567–574, 2003. DOI: [10.1115/1.1571080](https://doi.org/10.1115/1.1571080).
- [41] M. Zubair Akbar, M. Ashraf, M. Farooq Iqbal, and K. Ali, "Heat and mass transfer analysis of unsteady MHD nanofluid flow through a channel with moving porous walls and medium," *AIP Adv.*, vol. 6, no. 4, pp. 045222, 2016. DOI: [10.1063/1.4945440](https://doi.org/10.1063/1.4945440).
- [42] M. Sheikholeslami, D. D. Ganji, M. Y. Javed, and R. Ellahi, "Effect of thermal radiation on magnetohydrodynamic nano fluid flow and heat transfer by means of two-phase model," *J. Magn. Magn. Mater.*, vol. 374, pp. 36–43, 2015. DOI: [10.1016/j.jmmm.2014.08.021](https://doi.org/10.1016/j.jmmm.2014.08.021).
- [43] M. Sheikholeslami, M. Hatami, and D. D. Ganji, "Analytical investigation of MHD nanofluid flow in a semi-porous channel," *Powder Technol.*, vol. 246, pp. 327–336, 2013. DOI: [10.1016/j.powtec.2013.05.030](https://doi.org/10.1016/j.powtec.2013.05.030).
- [44] M. Sheikholeslami, M. Gorji-Bandpy, D. D. Ganji, P. Rana, and S. Soleimani, "Magnetohydrodynamic free convection of Al<sub>2</sub>O<sub>3</sub>–water Nano fluid considering Thermophoresis and Brownian motion effects," *Computers & Fluids*, vol. 94, pp. 147–160, 2014. DOI: [10.1016/j.compfluid.2014.01.036](https://doi.org/10.1016/j.compfluid.2014.01.036).
- [45] Q. Raza, *et al.*, "Mathematical modeling of nanolayer on biological fluids flow through porous surfaces in the presence of CNT," *Case Stud. Thermal Eng.*, vol. 45, no. 1, pp. 102958, 2023. DOI: [10.1016/j.csite.2023.102958](https://doi.org/10.1016/j.csite.2023.102958).
- [46] S. P. Jang and S. U. S. Choi, "Effects of various parameters on nanofluid thermal conductivity," *J. Heat Transf.*, vol. 129, no. 5, pp. 617–623, 2007. DOI: [10.1115/1.2712475](https://doi.org/10.1115/1.2712475).
- [47] R. Hentschke, "On the specific heat capacity enhancement in nanofluids," *Nanoscale Res. Lett.*, vol. 11, no. 1, pp. 88, 2016. DOI: [10.1186/s11671-015-1188-5](https://doi.org/10.1186/s11671-015-1188-5).
- [48] Q. Raza, *et al.*, "Significance role of dual porosity and interfacial nanolayer mechanisms on hybrid nanofluids flow: a symmetry flow model," *Mod. Phys. Lett. B*, vol. 38, no. 08, pp. 2450022, 2023. DOI: [10.1142/S0217984924500222](https://doi.org/10.1142/S0217984924500222).
- [49] G. Aaiza, I. Khan, and S. Shafie, "Energy transfer in mixed convection MHD flow of nanofluid containing different shapes of nanoparticles in a channel filled with saturated porous medium," *Nanoscale Res. Lett.*, vol. 10, no. 1, pp. 490, 2015. DOI: [10.1186/s11671-015-1144-4](https://doi.org/10.1186/s11671-015-1144-4).
- [50] M. M. Alanazi, *et al.*, "Numerical computation of hybrid morphologies of nanoparticles on the dynamic of nanofluid: the case of blood-based fluid," *Axioms*, vol. 12, no. 2, pp. 163, 2023. DOI: [10.3390/axioms12020163](https://doi.org/10.3390/axioms12020163).
- [51] S. Sindhu and B. J. Giresha, "Flow of colloidal suspension and irreversibility analysis with aggregation kinematics of nanoparticles in a microchannel," *Appl. Math. Mech.-Engl. Ed.*, vol. 41, no. 11, pp. 1671–1684, 2020. DOI: [10.1007/s10483-020-2669-9](https://doi.org/10.1007/s10483-020-2669-9).
- [52] H. Chen, Y. Ding, Y. He, and C. Tan, "Rheological behaviour of ethylene glycol based titania nanofluids," *Chem. Phys. Lett.*, vol. 444, no. 4–6, pp. 333–337, 2007. DOI: [10.1016/j.cplett.2007.07.046](https://doi.org/10.1016/j.cplett.2007.07.046).
- [53] J. Mackolil and B. Mahanthesh, "Sensitivity analysis of Marangoni convection in TiO<sub>2</sub>–EG nanoliquid with nanoparticle aggregation and temperature-dependent surface tension," *J. Therm. Anal. Calorim.*, vol. 143, no. 3, pp. 2085–2098, 2021. DOI: [10.1007/s10973-020-09642-7](https://doi.org/10.1007/s10973-020-09642-7).
- [54] J. Majdalani, C. Zhou, and C. A. Dawson, "Two-dimensional viscous flow between slowly expanding or contracting walls with weak permeability," *J. Biomech.*, vol. 35, no. 10, pp. 1399–1403, 2002. DOI: [10.1016/S0021-9290\(02\)00186-0](https://doi.org/10.1016/S0021-9290(02)00186-0).